Magneto-optical effects in lead halide perovskites

Yan Lv, Yuxiao Wang, Xueying Ma, Yao Xu, Lin Wang, Xiaoyong Wang, Min Xiao & Chunfeng Zhang

Published online: 25 Sep 2023.

Submit your article to this journal ⬚

Article views: 1049

View related articles ⬚

View Crossmark data ⬚

Taylor & Francis
Taylor & Francis Group

REVIEWS

 OPEN ACCESS Check for updates

Magneto-optical effects in lead halide perovskites

Yan Lv[a*], Yuxiao Wang[b*], Xueying Ma[b], Yao Xu[a], Lin Wang[a], Xiaoyong Wang[b], Min Xiao[b,c] and Chunfeng Zhang[b]

[a]School of Flexible Electronics (Future Technologies) & Institute of Advanced Materials, Key Laboratory of Flexible Electronics, Jiangsu National Synergetic Innovation Center for Advanced Materials, Nanjing Tech University, Nanjing, China; [b]National Laboratory of Solid State Microstructures, School of Physics, and Collaborative Innovation Center of Advanced Microstructures, Nanjing University, Nanjing, China and [c]Department of Physics, University of Arkansas, Fayetteville, AR, USA

ABSTRACT
Lead halide perovskites have emerged as promising semiconductors for high-performance photovoltaics, light-emitting devices as well as quantum information technologies. In this review, we highlight the magneto-optical effects in these materials from both fundamental research and practical application perspectives. We summarize the experimental results measured for basic physical quantities and the assignment of various spectral peaks using the magneto-optical spectroscopy. These results provide a solid foundation underlying the excellent photo-electronic properties of lead halide perovskites. Additionally, we provide an overview of carrier spin precession and its hyperfine interaction with the nuclear spin bath in response to the applied magnetic field, which is essential for developing perovskite-based spintronic devices. We also illustrate the magnetic-field effects in optoelectronic devices, aiming at providing instructions for performance optimization. Finally, we discuss several challenging research directions towards a comprehensive understanding of the perovskite family and their potential applications in quantum physics, which might be accessed with the magneto-optical techniques. Overall, this review highlights the intriguing possibilities for lead halide perovskites in magneto-optical research and technology, and provides insights for future investigations to advance this promising field.

CONTACT Yan Lv ✉ iamylv@njtech.edu.cn School of Flexible Electronics (Future Technologies) & Institute of Advanced Materials, Key Laboratory of Flexible Electronics, Jiangsu National Synergetic Innovation Center for Advanced Materials, Nanjing Tech University, Nanjing 211816, China
*These authors contributed equally to this work.
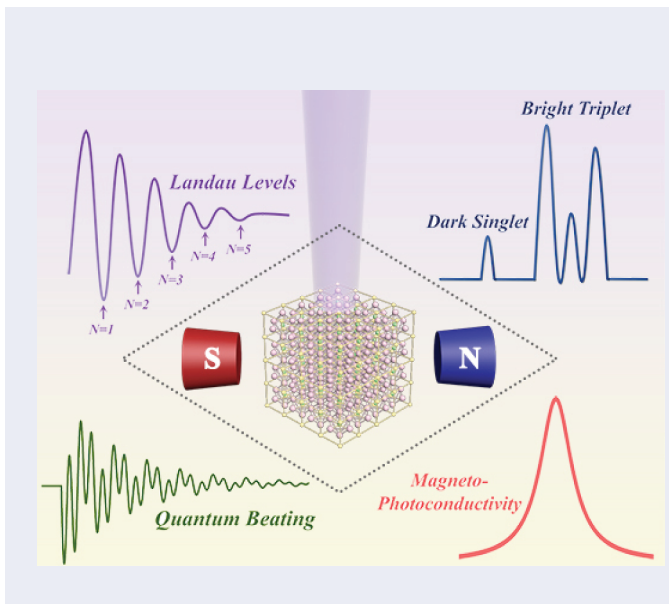
1. Introduction

Lead halide perovskite semiconductors with a flexible chemical composition of $APbX_3$ (e.g. A = Cs^+, MA^+ ($NH_3CH_3^+$), FA^+ ($CH(NH_2)_2^+$) and X = Cl^-, Br^-, I^-) have attracted huge attention in recent years for their superior optical and electronic characteristics, including broad bandgap tunability [1] [2,3], remarkable photoluminescence quantum yield [1,4–6], high defect tolerance [7–9], slow carrier recombination [10–13] and long diffusion length [14,15]. Unprecedented developments have been achieved for perovskite-based photovoltaics with the power conversion efficiency being raised from 3.8% to 25.7% [16–19], as well as for diverse optoelectronic applications such as light-emitting diodes [20–22], lasers [23–25] and photodetectors [26,27]. Furthermore, competitive exciton dephasing time exceeding hundreds of picoseconds [28,29] and spin coherence time of several nanoseconds [30,31] have been revealed, highlighting their great potentials in quantum information processing [32] and spintronic devices [33].

In order to maintain the impressive advancement as well as develop future multi-functionalized applications based on lead halide perovskites, it is of essential importance to establish comprehensive knowledge of fundamental electronic properties and accurate physical pictures for the energy-level structures that dominate the carrier formation, relaxation, transport and recombination processes [11,15,34,35]. Magneto-optical spectroscopy represents a valuable experimental tool to extract intrinsic physical properties of the materials in a straightforward manner. The Zeeman splitting and diamagnetic shift in the magnetic field, along with Landau levels in extremely high fields, yield intuitive information such as the carrier effective masses, the corresponding g-factors, the spatial extension of the wave functions and the

excitonic energy level structures, which may be difficult to access with other methods [36]. Meanwhile, magnetic field effects can be implemented to investigate the spin-dependent photon-to-charge interconversion photophysical processes in real optoelectronic devices by modulating the physical quantities, e.g. photoconductivity, electroluminescence and photoluminescence [37], paving the way for improving device efficiency as well as developing spin-related applications.

In this review, we focus on the magneto-optical effects in lead halide perovskites to elucidate the underlying physics of fundamental photoelectric properties and practical applications. In Section 2, we demonstrate the significance of the magnetic field in experimentally determining the material basic electronic parameters within both weak- and strong-field regimes, including exciton binding energy, carrier reduced mass and effective dielectric constant. In Section 3, the assignment of the complex band-edge exciton fine structures and phonon replicas with magneto-optical spectroscopy are comprehensively reviewed, with emphases on the field-induced state coupling and energy shifting. In Section 4, we outline recent breakthroughs in the coherent spin manipulation under external magnetic fields, including carrier spin precession and its hyperfine interaction with the nuclear spin bath. In Section 5, we discuss the magnetic field effects in perovskite optoelectronic devices to provide implications for performance optimization. These findings represent remarkable advances in understanding physical properties of lead halide perovskites, thus offering perspectives on potential research directions that may benefit from the magneto-optical effects.

2. Fundamental electronic parameters

Knowledge of the fundamental physical quantities such as the exciton binding energy (R^*), carrier reduced mass (μ) and effective dielectric constant (ε_{eff}) is vital for a thorough understanding of the electronic properties as well as performance improvement of perovskite-based applications. For instance, the exciton binding energy compared with the thermal energy (kT ~25 meV at 300 K) determines the operation behavior as excitons or free carriers in photoelectric devices, and the reduced mass intimately associated with key semiconductor characteristics like carrier mobility and diffusion length plays a dominant role in the carrier transport process.

Magneto-optical spectroscopy represents a powerful experimental approach enabling straightforward evaluation of the basic physical parameters mentioned above. In the presence of an external magnetic field, the orbital wave functions of charge carriers are localized to the plane perpendicular to the magnetic field and the resulting cyclotron motion is featured by the frequency of $\omega_c = eB/\mu$, where e is the electron charge, B is the magnetic field amplitude and μ is the exciton reduced mass given by $1/\mu = 1/m_e + 1/m_h$ (m_e and m_h are electron and hole effective masses, respectively). In the Faraday

configuration where the magnetic field is parallel to the light wave vector $(B\,||\,k,\ k\,||\,c)$, the Coulomb interaction in the exciton predominates when the cyclotron energy $\hbar\omega_c$ ($\hbar$ is the Planck's constant) is significantly smaller than the exciton binding energy R^*. In this case, the diamagnetic effect can be observed since the weak magnetic field can be treated as a perturbation to the exciton wave functions. However, the perturbation theory fails in the high magnetic field when $\hbar\omega_c \gg R^*$, under which the spectral features are governed by the free carrier Landau levels. A dimensionless parameter $\gamma = \hbar\omega_c/2R^*$ is introduced to distinguish the weak ($\gamma \ll 1$) and strong ($\gamma \gg 1$) magnetic field regimes [38].

2.1 Weak magnetic field regime

When the parameter γ is much smaller than unity ($\gamma \ll 1$), the magnetic field can be treated as a small perturbation acting on the exciton states. By adding the magnetic-field-involving terms to the total Hamiltonian and calculating the first-order perturbation solution, the modified energy of excitonic transitions can be derived [39]:

$$E_\pm = E_0 \pm \frac{1}{2}g_{eff}\mu_B B + c_0 B^2 \tag{1}$$

where E_0 is the unperturbed exciton energy, g_{eff} is the effective exciton Lande g-factor, μ_B is the Bohr magneton and c_0 is the diamagnetic coefficient. The second term in equation (1) describes the linear Zeeman splitting as a result of the magnetic-field-induced degeneracy lifting of excited states (see Figure 1(a)), while the third term represents the diamagnetic shift with the quadratic field dependence. For a comprehensive overview on the electronic states in magnetic fields as well as detailed derivation for equation (1), we refer readers to ref [39]. The diamagnetic coefficient c_0 is directly determined by the exciton reduced mass and the spatial extension of electron and hole wave functions [43,44]

$$c_0 = \frac{e^2}{8\mu}r^2 \tag{2}$$

where r^2 is the expectation value of the squared in-plane spatial extension. Under the assumption of hydrogen model, r^2 is proportional to $1/\mu^2$ and c_0 can be further described by [39]

$$c_0 = \frac{4\pi^2\varepsilon_{eff}^2\varepsilon_0^2\hbar^4}{\mu^3 e^2} \tag{3}$$

where ε_0 and ε_{eff} are the vacuum and effective dielectric constants, respectively. The exciton Bohr radius a_B, reduced mass μ and binding energy R^* can be expressed as [45]
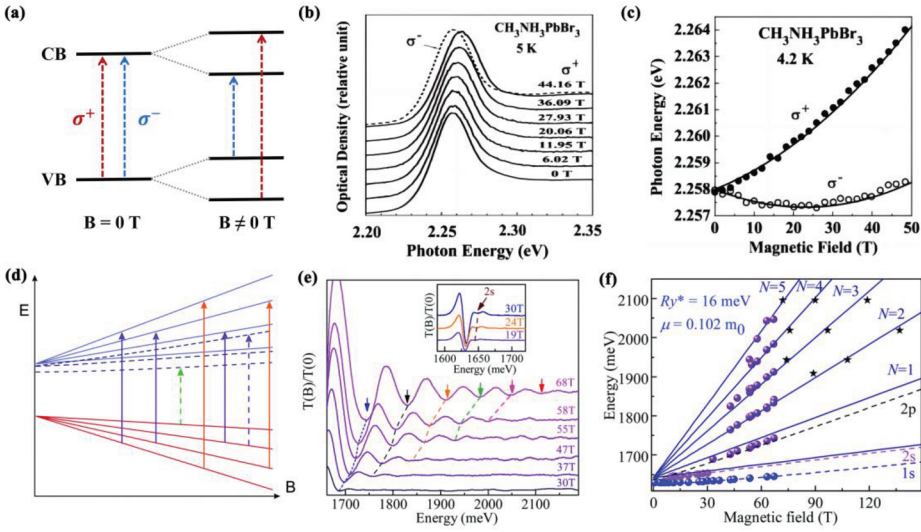
Figure 1. (a) A schematic view of Zeeman splitting in the magnetic field with the selection rules for circular polarizations. (b) Magneto-absorption spectra of MAPbBr$_3$ in the Faraday configuration. The spectra are shown for σ^+ polarization (solid lines) and σ^- polarization (dashed line). (c) Energy shifts as functions of the magnetic field in the Faraday configuration for MAPbBr$_3$. (b) and (c) Reproduced with permission from ref [40]. Copyright 2003, Elsevier Ltd. (d) A schematic view of the Landau levels (solid lines) and excitonic states (dashed lines) as a function of magnetic field. Reproduced with permission from ref [41]. Copyright 2016, Royal Society of Chemistry. (e) Sequences resonant absorption features in MAPbI$_3$ showing the free carrier Landau levels correspond to minima. (f) Fan chart plot of exciton and Landau-level energies as a function of magnetic field in MAPbI$_3$. The solid lines and the dashed lines are the fits to the set of Landau levels and the exciton transitions, respectively. Reproduced with permission from ref [42]. Copyright 2017, Royal Society of Chemistry.

$$\frac{a_B}{a_H} = \left(\varepsilon_{eff} \frac{c_0}{c_H} \right)^{\frac{1}{3}} \tag{4}$$

$$\frac{\mu}{m_e} = \left(\varepsilon_{eff}^2 \frac{c_H}{c_0} \right)^{\frac{1}{3}} \tag{5}$$

$$\frac{R^*}{R_H} = \left(\frac{c_H}{\varepsilon_{eff}^4 c_0} \right)^{\frac{1}{3}} \tag{6}$$

In these equations, $c_H = 1.23 \times 10^{-10}$ eV/T^2, $a_H = 0.53$ Å and $R_H = 13.6$ eV are the diamagnetic shift, Bohr radius and Rydberg constant of the hydrogen atom respectively, and m_e is the free electron mass. Provided that ε_{eff} is known, these fundamental exciton parameters can all be derived from the magnetic-field-induced diamagnetic shift.

Early magneto-absorption studies of lead halide perovskite crystals in the weak-field regime [40,43,45] were performed under the assumption of this hydrogen model to determine these physical quantities, as summarized in Table 1. In the Faraday configuration, the energy splitting between the σ^+ and σ^- exciton transitions and the energy shift of the absorption peak can both be observed as demonstrated in Figure 1(b), corresponding to the Zeeman splitting and diamagnetic shift, respectively [40]. The exciton energies plotted in Figure 1(c) exhibit the typical parabolic trend with the magnetic field, enabling the extraction of g_{eff} and c_0 by fitting the curves with equation (1). With the dielectric constant ε_{eff} set to be 4.8 for MAPbBr$_3$ and 6.5 for MAPbI$_3$, this work estimated the parameters of $a_B = 20$ Å, $\mu = 0.13$ m_e and $R^* = 76$ meV for MAPbBr$_3$ and $a_B = 22$ Å, $\mu = 0.15$ m_e and $R^* = 50$ meV for MAPbI$_3$. Smaller Bohr radius and larger exciton binding energy in MAPbBr$_3$, as compared to those in MAPbI$_3$, were attributed to the reduced dielectric screening of the electron-hole Coulomb interaction, due to the larger energy gap and the accompanied lower dielectric constant. It is not always necessary to choose the value of ε_{eff} in advance to calculate the electronic parameters. Recently, two distinct hydrogen-like exciton states with the energy of $E_i = E_g - \frac{R^*}{i^2}$ ($i = 1$, 2 and E_g is the bandgap energy) have been revealed by the low-temperature transmission spectroscopy of CsPbCl$_3$ films, leading to the direct determination of the exciton binding energy $R^* = 64$ meV. The magneto-optical experiments have been further involved to achieve the values of $\mu = 0.202$ m_e and $\varepsilon_{eff} = 6.56$ [46].

However, the simple approximation of c_0 proportional to $1/\mu^3$ in equation (3) may not be valid if the contributions of quantum confinement and dielectric confinement to the exciton spatial extension r^2 are considered, especially in two-dimensional (2D) perovskites. The exciton wave function cannot be strictly confined in plane when the perovskite layer thickness is comparable to r^2. Moreover, the reduced dielectric screening leads to the enhancement of the electron-hole Coulomb interaction, owing to the large dielectric constant ratio between the perovskite layer and the spacing layer [47]. Therefore, more complex models based on the first-principles calculations have been implemented to support the magneto-absorption spectra, and a monotonic decrease of μ from 0.221 m_e down to 0.186 m_e with the increasing layer thickness n from 1 to 5 can be deduced. The larger μ in 2D perovskites compared to their 3D counterparts was explained by the progressive reduction of the energy bandgap with the increasing n-value, while the binding energy of hundreds of meV is due to the strong dielectric confinement. In addition, the phase transition of 2D perovskites can induce a 30% increase of μ in the low-temperature phase, as proved by the significant variation of the diamagnetic shift coefficient c_0 [48]. The structural origin was interpreted as the different distortions of the [PbI$_4$]$^{2-}$ octahedral cages.

Table 1. Fundamental electronic parameters measured by magneto-optical spectroscopy in the weak-field regime. LT and HT denote low and high temperatures, respectively.

	Material	g_{eff}	c_0 (μeV/T^2)	a_B (nm)	R^* (meV)	μ (m$_e$)	ε_{eff}
Weak Magnetic Field Regime	MAPbBr$_3$ [40]	2.03	1.28	2.0	76	0.13	Set to be 4.8
	MAPbI$_3$ [40,45]	1.2	2.7	2.8	37	0.12	Set to be 6.5
		1.72	1.35	2.2	50	0.15	
	CsPbCl$_3$ [46]	0.8	0.64	/	64	0.202	6.56
	(C$_6$H$_{13}$NH$_3$)$_2$PbI$_4$ [43]	1.8	0.353	1.01	386	/	Set to be 3.68
	(BA)$_2$(MA)$_{n-1}$Pb$_n$I$_{3n+1}$ n = 1–5 [47]	0.8–1.6	0.2–1.1	/	470–125	0.221–0.186	4–5.2 and 2.2
	(C$_n$H$_{2n+1}$NH$_3$)$_2$PbI$_4$ n = 4, 6, 8, 10, 12 [48]	1.22–1.45 @LT 1.5–1.6 @HT	0.11–0.16 @LT 0.3–0.33 @HT	/	/	0.046 @LT 0.033 @HT	/

Despite the fruitful information provided by the magneto-optical spectroscopy in the weak field limit, it should be mentioned that the resulting electronic parameters were derived under the assumption of specific exciton models. Particularly, the uncertainty in the determination of ε_{eff} may bring about large deviations of a_B, μ and R^* from their true values.

2.2 Strong magnetic field regime

In contrast to the magneto-optical methods within the weak-field regime that require to presuppose specific exciton models or material parameter ε_{eff}, the interband Landau level transitions at high magnetic fields render direct measurements on the exciton reduced mass μ and binding energy R^* without any prior assumptions. When γ is much larger than unity ($\gamma \gg 1$), the system is almost Landau level-like and the Coulomb interaction is regarded as a small perturbation. To calculate the energy levels in this strong-field regime, the adiabatic approximation that decouples the in-plane and out-of-plane wave functions can be used and the magnetic field effect only acts on the in-plane component [39]. Based on this approach, the variations of the valence and conduction band-edge energies induced by the free carrier cyclotron motion can be calculated as $\Delta E = (N + 1/2) eB/m_{e,h}$, where $N = 0, 1, 2...$ represents the Landau orbital quantum number. Dipole-allowed transition occurs between the Landau levels with the same N as illustrated in Figure 1(d) and the corresponding transition energy is given by (neglecting the contribution from the Zeeman effect) [39]

$$E_N(B) = E_g + \left(N + \frac{1}{2}\right) \hbar\omega_c \qquad (7)$$

As a result, a sequence of evenly spaced spectral features above the bandgap can be resolved with the separation of $\Delta E_{N,N-1}(B) = \hbar\omega_c = \hbar eB/\mu$ (see Figure 1(e)), which enables precise extraction of the exciton reduced mass μ. The exact value of the bandgap E_g can also be deduced from extrapolation of the Landau levels to the zero magnetic field. To further achieve exciton binding energy R^*, a hydrogen-like numerical model in high magnetic fields developed by Makado and McGill can be employed, in which the dimensionless parameter $\gamma = \hbar\omega_c/2R^*$ is defined to describe the magnetic field dependence of energy levels $E(\gamma)$ [49]. With the knowledge of μ from the previous step, the only fitting parameter of this numerical model is R^*. Moreover, the energy of 1s and 2s exciton states place an additional strong constraint on the determination of R^*, which should be consistent with the zero-field eigenenergies of the 3D hydrogen-like exciton states given by $E_i = E_g - \frac{R^*}{i^2}$. Thus, the magnetic field dependence of near-band-edge exciton states and above-bandgap free-carrier transitions are simultaneously fitted to acquire an

accurate value of R^*, as shown in Figure 1(f). Finally, the effective dielectric constant can be derived by $\varepsilon_{eff} = \sqrt{(R_H \times \mu) / (R^* \times m_e)}$.

Optical transmission spectroscopy in high magnetic field up to ~150 T was first used by Miyata et al. to determine μ and R^* in an MAPbI$_3$ film [50]. The observation of 1s and 2s excitonic states along with the free carrier Landau levels leads to the values of $\mu = 0.104\ m_e$ and $R^* = 16$ meV for the low-temperature orthorhombic phase (see Table 2), significantly smaller than the results previously assumed using a low-magnetic-field approximation [40,45]. In the high-temperature tetragonal phase, an increase in the dielectric screening due to the activation of rotational motion of MA$^+$ cations [55] contributes to a smaller exciton binding energy of 12 meV [50], which was further supported by the magneto-reflectivity measurements on MAPbI$_3$ single crystals [51]. The negligible impact of microstructure on the Coulomb interaction between electron and hole was studied later by Soufiani et al. [42]. The thermal disorder on the electrostatic fluctuations and rotational dynamics of the unlocked organic cation are frozen at low temperatures, and thus μ and R^* remain unchanged in MAPbI$_3$ polycrystalline films with various morphologies. Extensive magneto-optical studies on MAPbBr$_3$ and MAPbI$_3$ as well as FAPbBr$_3$ and FAPbI$_3$ were reported to reveal that μ and R^* increase proportionally to the bandgap [41]. The detailed parameters are listed in Table 2 and are consistent with a semi-empirical k·p perturbation approach so that the prediction of μ and R^* for other members of perovskite compounds can be expected. Through partial substitution of the Pb by Sn, smaller μ and R^* can be gained with narrower energy bandgap [52]. The linear scale law of μ and R^* with energy bandgap has also been confirmed by the magneto-transmission measurements of fully inorganic CsPbX$_3$ perovskites [53]. Moreover, this work proved that the Pb-X stretching modes and Pb-X-Pb rocking modes in lead halide cage are the main factors that determine the dielectric permittivity in the low-temperature range. Measurements of the reduced mass in phenethylamine (PEA)-based 2D halide perovskites emphasized the effects of octahedra distortion imposed by the organic spacers and orbital hybridization controlled by the metal cation [54].

3. Energy-level structures

3.1 Band-edge excitons

The formation and radiative recombination of excitons (electron-hole pairs bounded by Coulomb interaction) underlie the luminescent properties of perovskites or indeed any semiconductors, and therefore are crucial for designing and optimizing the light-emitting and photonic devices [56,57]. The degeneracy of the band-edge exciton state is lifted by electron-hole exchange interaction, giving rise to several exciton sub-bands [58,59]. These so-called

Table 2. Fundamental electronic parameters measured by magneto-optical spectroscopy in the strong-field regime.

	Material	R^* (meV)	μ (m$_e$)	ε_{eff}
Strong Magnetic Field Regime	MAPbBr$_3$ [41]	25	0.117	7.5
	MAPbI$_3$ [41,42,51]	16	0.102	/
		16 @LT 12 @HT	0.104	9.4 @LT 10.9 @HT
		16 @LT 5–12 @HT	0.104	9.4 @LT 11–17 @HT
	MAPb$_{1-x}$Sn$_x$I$_3$ [52]	16	0.075–0.1	8.0–9.2
	FAPbBr$_3$ [41]	22 @LT 24 @HT	0.115 @LT 0.13 @HT	8.42 @LT 8.6 @HT
	FAPbI$_3$ [41]	14 @LT 10 @HT	0.09 @LT 0.095 @HT	9.35 @LT 11.4 @HT
	CsPbBr$_3$ [53]	33	0.126	7.3
	CsPbI$_2$Br [53]	22	0.124	8.6
	CsPbI$_3$ [53]	15	0.114	10
	(PEA)$_2$PbI$_4$ [54]	260	0.091	/

exciton fine structures in perovskites have been the subject of intense investigations [29,60–65], aiming at promoting their potential applications beyond the classical optoelectronic devices [56,66–68], to the regime of quantum information technologies [28,29,69,70].

The electronic band structure near the band gap of lead halide perovskites is mainly built from Pb and X atomic orbitals, with the conduction band edge based on the p-like orbitals of Pb and the valence band edge composed of Pb s-orbitals and X p-orbitals [55,71–73]. Strong spin-orbit coupling in the conduction band contributed by the heavy metal (Pb) splits the sextet manifold into doublet $J = 1/2$ (lower band) and quartet $J = 3/2$ (upper band) submanifolds, with J representing the total angular momentum. Therefore, the band-edge exciton is formed by the Coulomb interaction between a hole in the valence-band maximum states with $J^h = 1/2$, $J_z^h = \pm 1/2$ (projection on z) and an electron in the conduction-band minimum states with $J^e = 1/2$, $J_z^e = \pm 1/2$. The resulting four-fold degenerate exciton level is split by the electron-hole exchange interaction into a spin-forbidden dark singlet ($J = 0$, $|0_D$, $\Psi^1\rangle$) and a spin-allowed bright triplet ($J = 1$). Crystal field together with exchange interaction further lifts the degeneracy of the triplet states with lower crystal structure symmetries, such as tetragonal and orthorhombic phases, or in the case of shape anisotropy [38,74–76]. To be specific, the bright triplet in the tetragonal crystal structure is split into a doubly degenerate $|\pm 1\rangle$ state ($\Psi^{3\pm}$) coupled to circularly polarized light and a $|Z\rangle = |0_B$ state (Ψ^2) coupled to linearly polarized light with the electric vector along the z-axis. The former is further evolved to two in-plane orthogonal linearly polarized $|X\rangle = (|+1\rangle + |-1\rangle)/\sqrt{2}$ and $|Y\rangle = (|+1\rangle - |-1\rangle)/\sqrt{2}$ states ($\Psi^{X/Y}$) in the orthorhombic crystal structure. The schematic representation of the band-edge exciton fine structures is illustrated in Figure 2 [61].

It was speculated that the Rashba effect, the consequence of the inversion symmetry breaking in the crystal with strong spin-orbit coupling [77,78], would induce a reversion of the bright-dark level ordering in perovskite nanocrystals especially those with large sizes [29,79]. In 2D perovskite
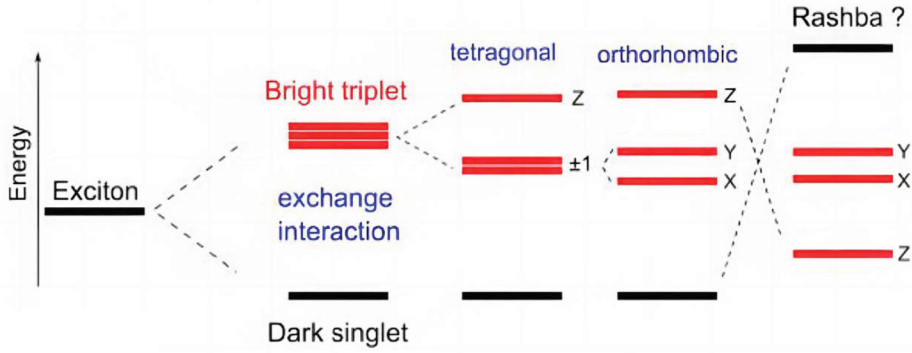
Figure 2. Energy-level diagram of the band-edge exciton fine structures resulting from electron-hole exchange interaction and crystal field splitting. The hypothetical Rashba effect might reverse the order of triplet and singlet states. Reproduced from ref [61]. Open access article distributed under the creative commons attribution license creativecommons.org/licenses/by/4.0/.

quantum-wells with strong dielectric confinement, the Rashba effect operates differently to cause a momentum splitting of an exciton spin-degenerate band with same energy [80,81], and the resulting two Rashba-split bands couple to the right and left circularly polarized photons, respectively.

3.2 Dark exciton state

Low-temperature magneto-optical spectroscopy plays an irreplaceable role in settling the debate on the bright-dark exciton level ordering in perovskite nanocrystals. The state-mixing effect induced by the magnetic field can transfer oscillator strength from the dipole-allowed to the dipole-forbidden transition, thus magnetically brightening the nominally inaccessible dark state [59,82].

In the Faraday configuration, the magnetic field mixes the dark Ψ^1 and out-of-plane Ψ^2 excitonic states, and promotes the in-plane $\Psi^{X/Y}$ states to proceed towards their genuine $\Psi^{3\pm}$ states with circular polarizations (see Figure 3(a)). The corresponding exciton eigenstates are

$$\phi_F^{1,2} = a_{1,2}\Psi^1 + b_{1,2}\Psi^2 \tag{8}$$

$$E_F^{1,2} = \frac{1}{2}\left[(E^1 + E^2) \pm \sqrt{(E^1 - E^2)^2 + (g_{e\parallel} - g_{h\parallel})^2 \mu_B^2 B^2}\right] \tag{9}$$

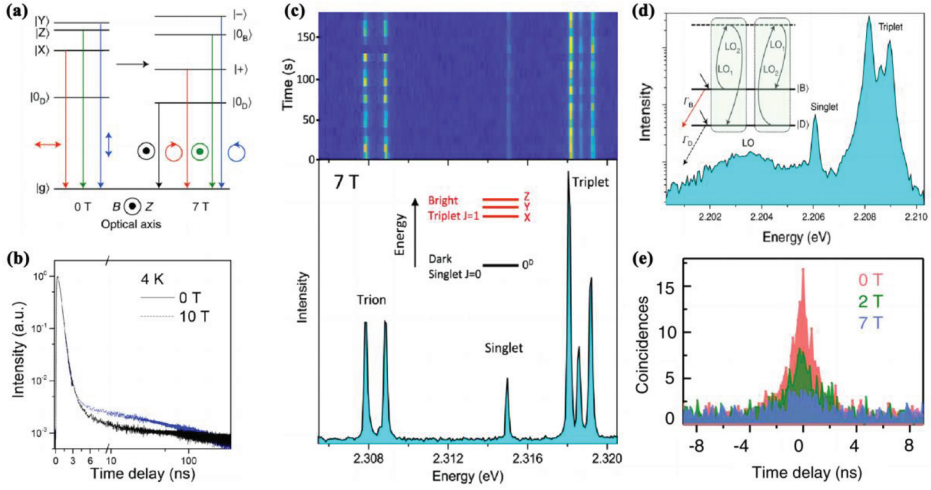$$\phi_F^{3\pm} = \boldsymbol{\Psi}^{3\pm} \tag{10}$$

Figure 3. (a) Scheme of fine structure splitting of the band-edge excitons in the Faraday configuration for a nanocrystal with an orthorhombic crystal structure. Reproduced with permission from ref [63]. Copyright 2019, Springer Nature Limited. (b) Time-resolved PL curves recorded from CsPbBr$_3$ nanocrystals at 4 K with and without an applied external magnetic field of 10 T. Reprinted with permission from ref [83]. Copyright 2018, American Chemical Society. (c) Spectral trail of a single CsPbBr$_3$ nanocrystal at 7 T (upper panel) and the spectrum integrated over the spectral trail showing a bright triplet, dark singlet and trion Zeeman doublet states at 7 T (lower panel). Reproduced with permission from ref [65]. Copyright 2023, Nature Publishing Group. (d) PL spectrum of a single FAPbBr$_3$ nanocrystal at 7 T displayed with a logarithmic scale in intensity to show the position of the weak optical phonon sideband with respect to the triplet and singlet sublevels. Inset: scheme of the two-phonon thermal mixing model between the dark state and one bright state. Reproduced with permission from ref [63]. Copyright 2019, Springer Nature Limited. (e) Photon coincidence histograms of a single CsPbI$_3$ nanocrystal at various magnetic fields at 4 K, showing the weakening of the bunching effect with increasing magnetic fields. Reproduced with permission from ref [64]. Copyright 2020, Nature Publishing Group.

$$E_F^{3\pm} = E^3 \pm \left(g_{e\parallel} + g_{h\parallel} \right) \boldsymbol{\mu}_B B \tag{11}$$

where $a_{1,2}$ and $b_{1,2}$ are coefficients depending on the magnetic field B, the spin-orbit coupling, the crystal field and the energy splitting between the $\mathbf{\Psi}^1$ and $\mathbf{\Psi}^2$ states [36,38,43,84], $g_{e\parallel}$ and $g_{h\parallel}$ are the electron and hole g-factors along B, respectively [38]. Hence the dark $\mathbf{\Psi}^1$ state gains oscillator strength from the $\mathbf{\Psi}^2$ state that is linearly polarized along the optical axis, which can be collected by a high numerical objective.

The low-lying dark singlet state was initially evidenced by the photoluminescence (PL) dynamics of perovskite nanocrystal ensembles in the magnetic field at cryogenic temperatures [83,85]. Typical time-resolved PL curves depicted in Figure 3(b) show a bi-exponential decay with a dominant fast component (hundreds of picoseconds) and a slow component (tens to hundreds of nanoseconds) [83]. The characteristic time of the latter shortens

distinctly with the magnetic field, while its contribution to the total PL intensity grows considerably. Using the three-level model proposed previously in colloidal CdSe nanocrystals [59,82], it was estimated by Chen et al. that the dark state in $CsPbBr_3$ nanocrystals is located ~7.7 meV below the bright states. This energy splitting is highly sensitive to both halide elements and organic cations, which change the exchange interactions by size confinement and charge screening, respectively [83].

By applying an external magnetic field of 7 T in the Faraday configuration, the direct spectroscopic signature of dark exciton emission was first provided by Tamarat et al. in the low-temperature PL measurements of single $FAPbBr_3$ nanocrystals [63], with the follow-up research on single $CsPbI_3$ [64] and $CsPbBr_3$ [65] nanocrystals by the same group (see Figure 3(c)). A field-induced red-shifted emission line emerges in the PL spectrum regardless of the triplet structure, and it can be unambiguously attributed to the ground dark singlet exciton state. The energy splitting between the dark and bright states has been reported to be ~2.5 meV for $FAPbBr_3$ nanocrystals with an average size of 9.2 nm [63], ~5 meV for $CsPbI_3$ nanocrystals with an average size of 11.2 nm [64] and at least 3.6 meV for nearly-bulk $CsPbBr_3$ nanocrystals [65], which are at variance with the theoretical models based on Rashba effects [29,79,86]. Furthermore, a universal scaling law relating the bright-dark splitting to the band-edge exciton energy in lead halide perovskite nanocrystals has been unveiled, supporting the picture that the exciton fine structures are dominated by the electron-hole exchange interaction under the combined effects of quantum confinement and screening of the electron-hole interaction. As illustrated in Figure 3(d), two-phonon-assisted thermal mixing model involving absorption and emission of longitudinal optical (LO) phonons was proposed to explain the reduced relaxation rate between dark and bright states, rationalizing the intense emission with such level ordering [63,64,87]. Interestingly, the long-lived dark singlet state is proved to promote the creation of biexcitons at low temperatures, and thus the magnetic-field-induced state-mixing effect can be used to tune the photon statistics of single quantum emitters (see Figure 3(e)) [65].

Magnetic brightening of the lowest dark state in 2D perovskites PEA_2PbI_4 single crystals has also been reported, which is separated by 15.5 meV from the bright excitonic states in the Faraday configuration [88]. Manganese doping can further enhance the bright-dark state mixing in the existence of magnetic field, either by accelerating the bright-dark relaxation rate or by forming an additional radiative recombination channel involving the spin-flip mediated by Mn^{2+} [89].

The Voigt configuration in which the in-plane magnetic field is perpendicular to the light wave vector, i.e. $B \perp k$, $k||c$, can be more beneficial to access the optically-forbidden dark state. The out-of-plane $\mathbf{\Psi}^1$ and $\mathbf{\Psi}^2$ exciton states are mixed with the in-plane $\mathbf{\Psi}^{3\pm}$ states in the Voigt configuration, leading to two
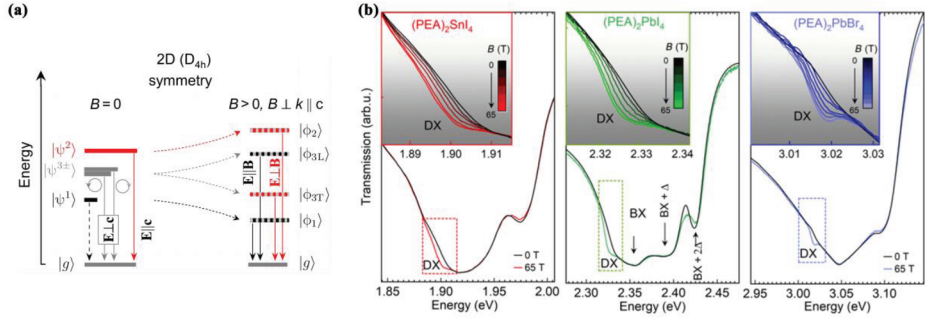
Figure 4. (a) Scheme of fine structure splitting of the band-edge excitons in the Voigt configuration. (b) Transmission spectra of 2D perovskites at zero magnetic field (black) and at B = 65 T (colored lines) for $(PEA)_2SnI_4$, $(PEA)_2PbI_4$, and $(PEA)_2PbBr_4$, respectively. Inset shows an expanded view of the evolution of the dark state (DX) with increasing magnetic field. Reproduced with permission from ref [90]. Copyright 2021, American Association for the Advancement of Science.

pairs of in-plane states with orthogonal linear polarizations. One pair characterized by the dipole moment along B is labeled as longitudinal, while the other pair with the dipole moment perpendicular to B is labeled as transverse. The corresponding exciton eigenstates are

$$\phi_V^{1,3L} = c_{1,3L}\mathbf{\Psi}^1 + d_{1,3L}(\mathbf{\Psi}^{3+} - \mathbf{\Psi}^{3-}) \tag{12}$$

$$E_V^{1,3L} = \frac{1}{2}\left[(E^1 + E^3) \pm \sqrt{(E^3 - E^1)^2 + (g_{e\perp} - g_{h\perp})^2\boldsymbol{\mu}_B^2 B^2}\right] \tag{13}$$

$$\phi_V^{2,3T} = c_{2,3T}\mathbf{\Psi}^2 + d_{2,3T}(\mathbf{\Psi}^{3+} + \mathbf{\Psi}^{3-}) \tag{14}$$

$$E_V^{2,3T} = \frac{1}{2}\left[(E^2 + E^3) \pm \sqrt{(E^3 - E^2)^2 + (g_{e\perp} + g_{h\perp})^2\boldsymbol{\mu}_B^2 B^2}\right] \tag{15}$$

where the coefficients $c_{1,3L}$, $d_{1,3L}$, $c_{2,3T}$ and $d_{2,3T}$ are functions of the magnetic field B, the splitting of the exciton states and the effective g-factors, while $g_{e\perp}$ and $g_{h\perp}$ are the respective electron and hole g-factors along B [90]. Therefore, the magnetic field transfers oscillator strength from the $\mathbf{\Psi}^{3\pm}$ to $\mathbf{\Psi}^{1,2}$ states, which can be observed conveniently under in-plane linear polarizations, as depicted in Figure 4(a).

A bright-dark splitting ranging from 28 to 32 meV was measured in $(C_4H_9NH_3)_2PbBr_4$, which is significantly enhanced as a result of strong

dielectric confinement, or image charge effect in 2D quantum wells [91]. Magneto-transmission spectroscopy in the Voigt configuration performed by Dyksik et al. leads to the direct observation of the low-lying dark state in 2D perovskites, with the results displayed in Figure 4(b) [90]. It has been revealed that the measured splitting is an order of magnitude larger than that in 3D perovskite nanocrystals [63–65] which is in agreement with the enhanced excitonic effects in these 2D quantum wells, while the correlation between the splitting and the exciton binding energy still stands.

3.3 Bright-exciton fine structure splittings

The physics of bright-exciton fine structure splittings in lead halide perovskites has attracted extensive research interest [29,60–62,76,88,92,93] for its potential as an efficient platform to coherently manipulate wave functions [69,94] and exploit quantum logic gates [95]. As reviewed previously, the magnetic field effect serves as a unique tool to reveal the exciton fine structures, and the response of the bright triplet will be elaborated as follows.

Single perovskite nanocrystals with different structural symmetries exhibit single, doublet or triplet peaks of exciton luminescence, typically with linear polarizations as a consequence of the electron-hole exchange interaction and the crystal field [63,64,76,96]. Under the magnetic field in the Faraday configuration, the genuine bright eigenstates, two of which featured by right- and left-handed circular polarizations ($\Psi^{3\pm}$) and the other one linearly polarized along the z-axis (Ψ^2), can be unveiled once the Zeeman effect exceeds the zero-field splitting as demonstrated in Figure 5(a–c) [64]. For those single nanocrystals with doublet peaks, the orientation, i.e. the crystal axis z with respect to the magnetic field c, can be restored by analyzing the evolution of PL spectrum with the magnetic field. As exemplified in Figure 5(d, e), the doublet will evolve into triplet as the originally degenerate states $\Psi^{X/Y}$ go through Zeeman splitting for nanocrystals with a symmetry axis along the field, while no extra peak will emerge for those having a symmetry axis perpendicular to the field [96]. Magnetic-field-induced excitonic states with circular polarizations by the Zeeman effect were observed in bulk 3D and 2D single crystals as well [43,45,65,88,92,93], and the resulting unbalanced population between the spin-up and spin-down sublevels renders spin polarization control towards spintronic devices [88,89,97].

The intrinsic origin of bright-exciton zero-field splitting, which is hundreds of μeV in nanocrystals [29,60,64,98] and single crystals [65,88] and can be as large as several meV in 2D perovskites [93], has been under the debate. A nonlinear energy splitting versus magnetic field strength in a single CsPbBr$_3$ nanocrystal, together with the coexistence of both linear and circular polarizations of the same optical transition, was considered as the competition of Rashba effect and Zeeman effect [98]. Symmetry breaking by a surface effect
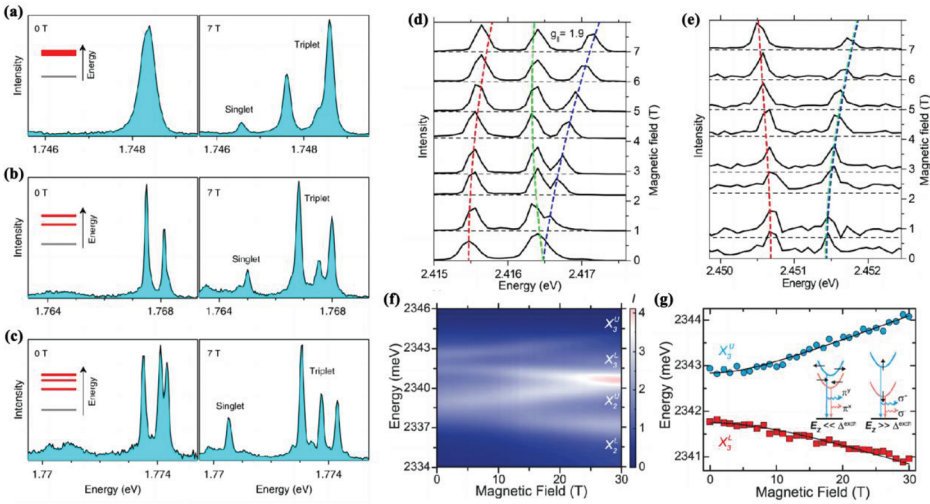
Figure 5. (a)-(c) Magnetic splitting and coupling among the fine structure sublevels in single CsPbI$_3$ nanocrystals with different crystal structures, revealing the entire spectral fingerprint of the bright triplet and the lowest-energy singlet state. The insets show the corresponding diagrams of exciton fine structures. (a)-(c) Reproduced with permission from ref [64]. Copyright 2020, Nature Publishing Group. (d) and (e) PL spectra of two types of CsPbBr$_3$ nanocrystal under magnetic fields ranging from 0 to 7 T. (d) and (e) Reprinted with permission from ref [96]. Copyright 2017, American Chemical Society. (f) Intensity mapping of the unpolarized PL spectra in PEA$_2$PbI$_4$ in magnetic fields from 0 to 30 T. (g) Energies of X_3^U (blue circles) and X_3^L (red squares) in PEA$_2$PbI$_4$ as a function of B. Inset: scheme illustrating the polarization and spin configurations of the exciton sub-bands at low-field and high-field limits. (f) and (g) Reprinted with permission from ref [93]. Copyright 2020, American Chemical Society.

or a lattice distortion induced by the Cs$^+$ motion, combined with internal spin-orbit coupling, satisfies the conditions for the Rashba effect, which is dominant in the zero and low magnetic field under 4 T to cause a splitting between the singlet and triplet states. At large magnetic fields, the Zeeman effect contributes to the linear response of fine structure splitting with the magnetic field. However, the Rashba origin remains hypothetical since the dark singlet virtually lies under the bright triplet [63–65,88,90], overturning the speculation of the Rashba-induced bright-dark state reversion [29,79]. In the meantime, it has been declared that the electron-hole exchange interaction combined with symmetry considerations should be responsible for the zero-field fine structure splitting [63–65,92,93]. A universal scaling law has been unraveled in Ref. 33 to describe the energy splitting between the exciton sublevels as a function of the exciton quantum confinement contributed by the long- and short-range exchange interactions. In the case of 2D perovskites, the energy fine structures were also tracked under the magnetic field in the Faraday configuration, as illustrated in Figure 5(f, g) [93]. The energy splitting up to 2 meV between the upper and lower bands was interpreted as a consequence of the exchange interaction, since the Rashba effect only cause the momentum mismatch of a spin-degenerate band without energy splitting in 2D perovskites [80,81,93].

3.4 Phonon replicas

The intrinsic soft ionic lattice of semiconductor perovskites is featured with diverse vibrations, bringing about distinct exciton-phonon interaction that plays a nonnegligible role in the hot carrier cooling and charge transport [11,13,99–101]. These lattice vibration modes also manifest themselves in spectra as phonon replicas or sidebands when the optical transition is assisted by absorbing or emitting a phonon [28,48,54,87]. Magnetic-optical spectroscopy can be helpful to assign the complex absorption, transmission or PL peaks when multiple phonons with different characteristic energies are involved with the original excitonic transition. A series of dips with equal spacing of 15 meV were observed in the transmission spectra of $(C_6H_{13}NH_3)_2PbI_4$, and were attributed to phonon replicas induced by Pb-I vibration as verified by their evolution under the magnetic field [48]. Since the lattice vibrations are unaffected by the magnetic field, the phonon replicas should track the evolution of the excitonic peak. The phonon-assisted absorption states in PEA_2PbI_4 were also confirmed by the second derivative of the σ^+ and σ^- spectra at 65 T, which show the same energy shift in magnetic field [54]. Exciton-phonon coupling in $(PEA)_2(MA)_{n-1}Pb_nI_{3n+1}$ was investigated by Urban et al. with magneto-absorption spectroscopy to reveal a vibronic progression of excitonic transition [102]. Additional peaks in the higher energy side of 1s transition behave uniformly in the magnetic field with the same diamagnetic shift, as validated by the perfect overlap of the spectra measured at 0 T and 65 T see Figure 6(a, b). These results reinforce the phonon-replica assignment and the sidebands with ~40 meV for all samples with different n ($n = 1, 2, 3$) should be related to the PEA ligand vibrations.

Polarons, quasi-particles formed from electronic excitations dressed by lattice vibrations [104,105], have been proposed to be responsible for many exotic optoelectronic properties in perovskites such as defect tolerance, moderate charge carrier mobility and reduced carrier cooling rate [106–109]. Several proofs obtained by magneto-optical measurements have been claimed to support the polaron picture. An effective mass of $\mu = 0.185\, m_e$ has been determined by the low-field diamagnetic shift in $MAPbBr_3$ single crystals [92], which is significantly deviated from the value deduced by the free electron Landau levels in high magnetic fields [41]. The larger reduced mass was regarded as a hallmark of polaronic effects contributed by the strong electron-phonon coupling in perovskites. Multiple PL structures with dominant intensity in PEA_2PbI_4 single crystals have also been ascribed to the exciton-polaron emission [88]. These red-shifted PL bands exhibit the same linear polarization and magnetic field induced shift as the free exciton transitions, while no corresponding transitions can be found in the reflectance response. Therefore, the authors hypothesized that the dominant PL emission should be linked to specific lattice reorganizations provoked by free
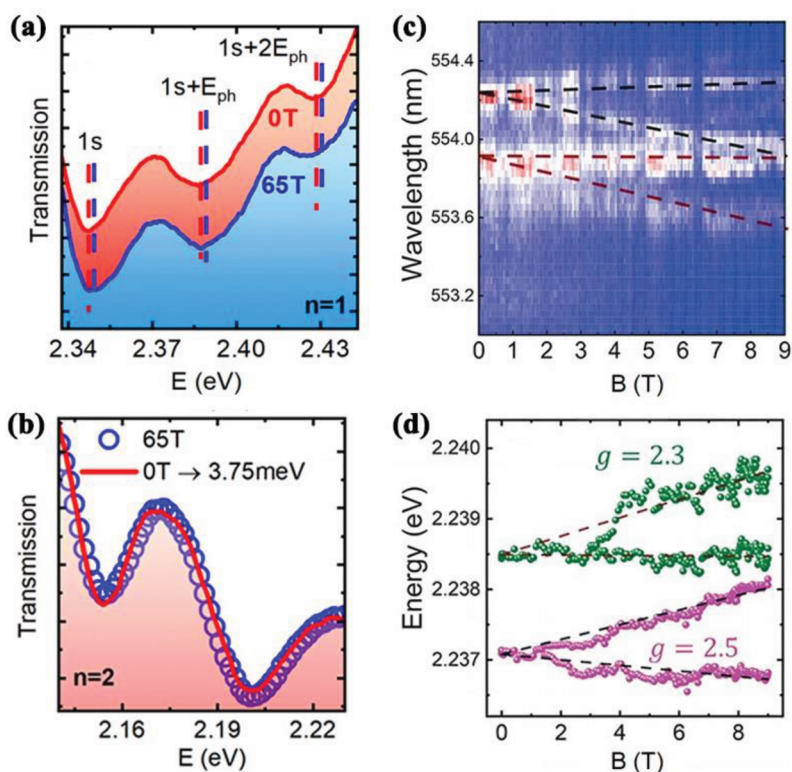
Figure 6. (a) 4 K transmission spectra measured at 0 T (red) and 65 T (blue) for PEA_2PbI_4. (b) Diamagnetic shift obtained for $PEA_2MAPb_2I_7$ by shifting the 0 T spectra (red curve) to obtain perfect overlap with the 65 T spectra (open circles). The two features exactly track each other in magnetic field. (a) and (b) Reprinted with permission from ref [102]. Copyright 2020, American Chemical Society. (c) Magneto-PL map of the zero-phonon line (black dashed) and polaron (wine dashed) in $MAPbBr_3$ nanowires. (d) The extracted peak energies in (c) and the corresponding g-factors. Reprinted with permission from ref [103]. Copyright 2019, Wiley-VCH Verlag GmbH & Co. KGaA, Weinheim.

excitons. In $MAPbBr_3$ nanowires, several PL peaks (up to 13) with narrow linewidths appeared at the high energy side of the zero-phonon line (ZPL) and were attributed as hot polarons, which originate from the interaction between localized excitons and transverse optical phonons [103]. Magneto-optical spectra were applied to confirm the polaron origin. As demonstrated in Figure 6(c, d), Zeeman splitting of the first polaron and the corresponding g-factors similar to those of ZPL can be observed clearly, while the phonon energy calculated by subtracting the energy of ZPL from first polaron increases with a value of 0.5 meV at 9 T. The diamagnetic effect was explained by the modified phonon wave vector that offsets the electron momentum with the vector potential to maintain momentum conservation, and the involved phonon mode corresponds to octahedra-twist vibrations. Despite the limited report relating the magnetic-field effects of polarons, unique control of excitonic system impacted by lattice deformation can be expected in lead halide perovskites.

4. Coherent spin dynamics

4.1 Spin precession

When two or more near-degenerate transitions are excited with a short optical pulse, whose spectral width is sufficiently large to 'cover' these eigenstates, a coherent superposition state will be generated to induce sinusoidally oscillating and exponentially decaying signals [110,111]. The oscillation frequencies are related to the slightly different transition energies while the decay rates depend on the decoherence processes. This so-called quantum beating reveals coherent spin dynamics of excitons/carries and leads to accurate measurements of the corresponding g-factors, decoherence times and energy level structures [111].

The strong spin-orbit coupling in lead halide perovskites enables efficient optical orientation and manipulation of carrier spin states [112–114], together with their impressive long spin lifetimes [31,115–117], making these materials promising candidates in spintronic applications [118,119]. Time-resolved Faraday rotation (TRFR) measurements in magnetic fields have been employed to explore spin-dependent physics in both perovskite bulks [31,115,120–122] and nanocrystals [116,117], with the working principle depicted in Figure 7(a). A resonant circularly polarized pump pulse generates coherent superposition of the spin states, which produces quantum beating in a transverse magnetic field (Voigt geometry), and can be detected via optical Faraday rotation of a linearly polarized probe pulse. This phenomenon has also been described as spin precession, and its dependence on the magnetic field yields information of carrier g-factors (g_e and g_h) and transverse spin dephasing time (T_2^*).

The experimental fulfillment of spin-polarized exciton quantum beating was first demonstrated by Odenthal et al. in perovskite $MAPbCl_xI_{3-x}$ polycrystalline films at cryogenic temperatures [31], and soon after several studies were reported to elucidate thoroughly coherent spin dynamics in lead halide perovskites [115–117,120–122]. A small magnetic field in the Voigt configuration results in the Larmor precession of carrier spin polarization with the frequency $\omega_{L,e(h)} = |g_{e(h)}| \mu_B B_V/\hbar$ [123], and therefore the oscillation signals in TRFR can be observed, with typical results shown in Figure 7(b) [115]. The Faraday rotation dynamics can be fitted well by the sum of two oscillations that decay exponentially:

$$\theta_F(t) = A_e e^{-t/T_{2,e}^*} cos(\omega_{L,e}t + \phi_e) + A_h e^{-t/T_{2,h}^*} cos(\omega_{L,h}t + \phi_h) \quad (16)$$

where $A_{e(h)}$ is the amplitude of electron (hole) spin signal and $T_{2,e(h)}^*$ denotes the transverse spin dephasing time of electron (hole).
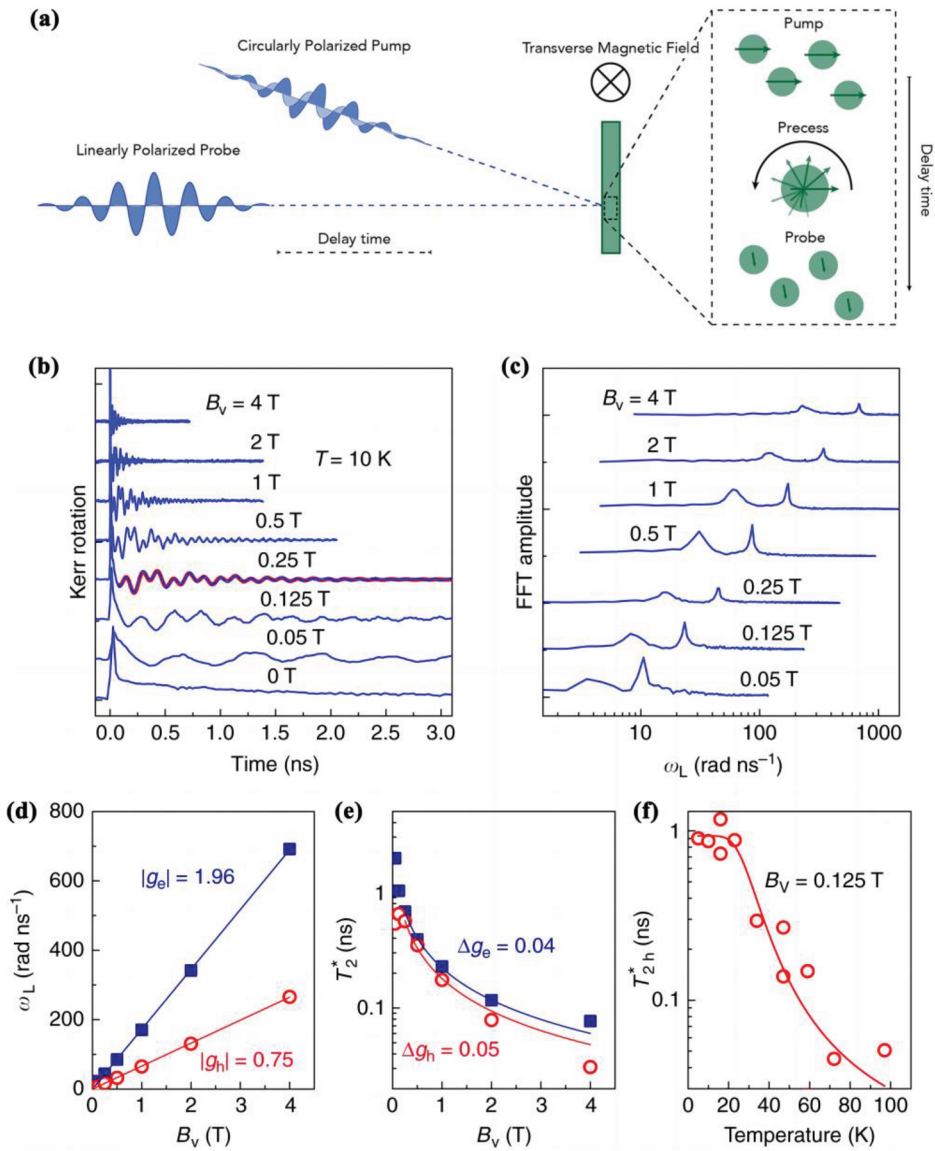
Figure 7. (a) Schematic summary of the time-resolved Faraday rotation experiment in the transverse magnetic field. Reprinted with permission from ref [116]. Copyright 2020, American Chemical Society. (b) Kerr rotation dynamics in CsPbBr$_3$ crystal at different magnetic fields. (c) Fast Fourier transform spectra of spin dynamics traces from (b). (d) Magnetic field dependencies of electron (squares) and hole (circles) Larmor frequencies. (e) Magnetic field dependencies of electron (squares) and hole (circles) spin dephasing times. (b)-(e) $T = 10$ K. (f) Temperature dependence of hole spin dephasing time. (b)-(f) Reproduced with permission from ref [115]. Copyright 2019, Nature Publishing Group.

Two distinct Larmor frequencies $\omega_{L,e(h)}$ can be evidenced as well by the fast Fourier transform spectra in Figure 7(c) and grow linearly with the magnetic field, which enables the extraction of the electron and hole g-factors

(see Figure 7(d)). Due to the variation between the bandgaps, the obtained carrier g-factors may present different magnitude and even sign for different perovskite materials [121]. For instance, the g-factors are $g_e = +1.73$ for electrons and $g_h = +0.83$ for holes in $CsPbBr_3$ nanocrystals [117], while the values of $g_e = +3.57$ and $g_h = -1.21$ have been calculated for $FA_{0.9}Cs_{0.1}PbI_{2.8}Br_{0.2}$ single crystals [120]. The universal formula of the carrier g-factors depending on the bandgap energy has been established by theoretical approaches based on the density functional theory and empirical tight-binding method [121]. The g-factor anisotropy has also been investigated to reveal the information on the crystal symmetry by tilting the magnetic field in a vector magnet, which concludes that the conduction band crystal splitting mainly influences g_h and the anisotropy of the interband momentum matrix elements affects both g_e and g_h [121].

Another key parameter given by the fitting of Eq. 16 is the transverse spin lifetime T_2^* that characterizes the spin dephasing and decoherence processes in the materials. In an ensemble of carrier spins, the phase difference between spins with different Larmor precession frequencies develops fast in time. As a result, the frequency dispersion leads to the additional inhomogeneous dephasing process and the decoherence is faster in the macroscopic spin system than the individual spin. Under the external magnetic field, the inhomogeneous dephasing time is due to variations of the carrier g-factors and has a $1/B$ dependence, which is given by $\hbar/\Delta g_{e,h}\boldsymbol{\mu}_B B_V$ [111]. As shown in Figure 7(e), T_2^* shortens with the magnetic field strength as a result of the g-factor dispersion $\Delta g_{e,h}$ contributed by the sample inhomogeneity and anisotropy [31], and the relation can be described as

$$1/T_2^*(B) = 1/T_2^*(0) + \Delta g_{e,h}\mu_B B_V/\hbar \tag{17}$$

The $\Delta g_{e,h}$ obtained for electrons and holes is of the same magnitude in bulk and nanocrystals [31,115–117,120], pointing to the indecisive impact of the crystal structure and nanocrystal orientations on the g value heterogeneity [116]. More importantly, the spin dephasing time at zero magnetic field $T_2^*(0)$ can exceed 1 ns at cryogenic temperatures [31,115,117,120] despite the existence of the large spin-orbit coupling, indicating their great potentials for quantum information processing to manipulate solid-state spin coherence [124,125]. Indeed, optical initialization, manipulation and readout of hole spins in surface functionalized $CsPbBr_3$ nanocrystal ensembles have been realized at room temperature [126].

Temperature dependence of coherent carrier spin dynamics in perovskites has also been investigated to gain insights of the spin decoherence mechanisms, such as the phonon-modulated hyperfine field effect, the Elliott-Yafet mechanism and the Dyakonov-Perel mechanism [31,115–117,120]. In bulk materials, T_2^* calculated from the TRFR signals in the magnetic field shows

an apparent decrease with the elevated temperature, as demonstrated in Figure 7(f), which exhibits an activation-type dependence [115,120]:

$$1/T_2^*(T) = 1/T_{2,0}^* + we^{-\Delta E/k_B T} \tag{18}$$

In the above equation, $T_{2,0}^*$ denotes the spin dephasing lifetime at zero temperature, w is the phenomenological factor that characterizes the strength of carrier-phonon interaction, ΔE is the activation energy and k_B is the Boltzmann constant. This Arrhenius-like relationship describes thermally activated spin dephasing with a temperature dependence, which may be related to the hole delocalization or LO-phonon-mediated spin-flip process [115,116,120]. However, it has been reported that the carrier spin dephasing time in $CsPbBr_3$ nanocrystals shows slight change in the temperature range below 35 K, which has been attributed to the carrier localization in quantum-confined nanocrystals [117].

4.2 Hyperfine interaction

The carrier-nuclei interaction that dominates the coherent spin dynamics at low temperatures and weak magnetic fields has also been explored in lead halide perovskites [115–117,120]. By suppressing the hyperfine interaction with a small magnetic field of 0.13 T, the hole transverse spin dephasing time $T_{2,h}^*$ in $CsPbBr_3$ nanocrystals can be 300% increased to 292 ps, which approaches the PL lifetime of 312 ps (see Figure 8(a)) [116]. As a comparison, only 20% increase of $T_{2,h}^*$ from 0 T to 0.125 T has been achieved in bulk $CsPbBr_3$ [115]. The different magnetic field response may stem from the confinement-enhanced hyperfine interaction in nanocrystals, where the surrounding nuclear spin bath, e.g. from proton-bearing surface ligands and polymer matrices, has more remarkable impacts on the carrier spin dephasing [116,127–129]. Furthermore, the temperature dependence of $T_{2,h}^*$ measured with and without magnetic field displayed in Figure 8(b) unambiguously elucidates two spin dephasing mechanisms. Specifically, the magnetic-field-dependence of $T_{2,h}^*$ below 50 K corresponds to the efficient compensation of the inhomogeneous nuclear spin fluctuations that predominate the spin dephasing at low temperatures, while the temperature-dependence of $T_{2,h}^*$ above 100 K is attributed to the the coupling of the carrier spins and LO phonons [116].

Quantitative evaluation of the effective hyperfine field strength has also been reported in the literature [115,117,120]. The carrier spin polarization produces Knight field that acts on the nuclear spin system by flip-flop hyperfine process, and the polarized nuclei induce the Overhauser field in turn
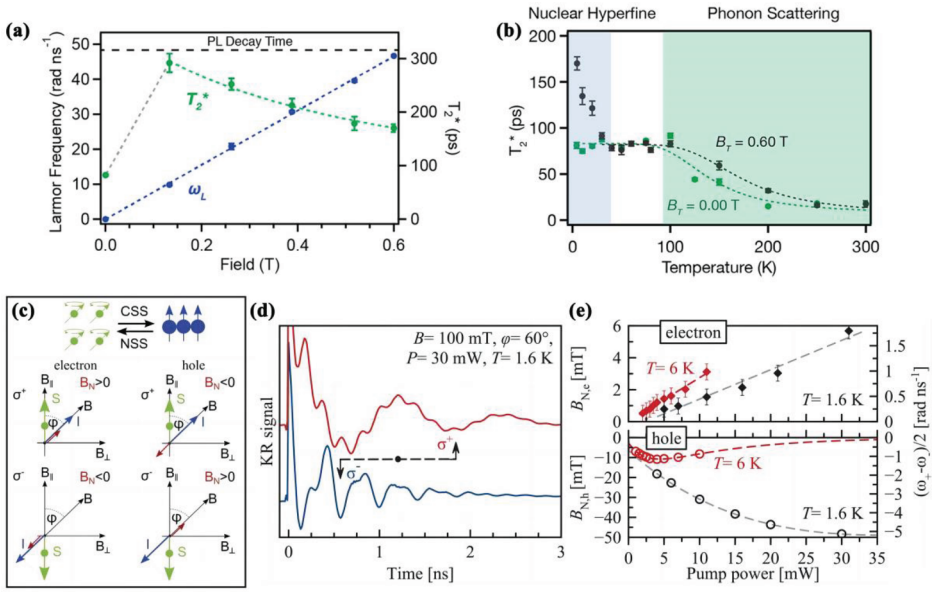
Figure 8. (a) Dependence of the Larmor frequency ω_L (blue) and ensemble spin-dephasing time T_2^* (green) for CsPbBr$_3$ nanocrystals on the transverse magnetic-field strength. The gray dashed line between 0 and 0.16 T is a guide to the eye. For comparison, the black horizontal dashed line shows the PL decay time (312 ps) measured at 4.5 K under the same conditions. (b) Ensemble inhomogeneous transverse spin-dephasing times T_2^* measured for CsPbBr$_3$ nanocrystals with and without an applied magnetic field, plotted as a function of sample temperature. (a) and (b) Reprinted with permission from ref [116]. Copyright 2020, American Chemical Society. (c) Scheme of interaction of carrier spin system (CSS) and nuclear spin system (NSS). (d) TRFR with σ^+ (red) and σ^- (blue) pump. The Overhauser field is either parallel or antiparallel to the external magnetic field. The arrows indicate the time shift of the second minimum of the hole spin Larmor precession. (e) Dependence of $B_{N,e(h)}$ on pump power at $T = 1.6$ K (black) and 6 K (red). Right scale shows the change of Larmor frequency. (c)-(e) Reproduced with permission from ref [120]. Copyright 2021, John Wiley & Sons, Ltd.

to influence the carrier behavior. Experimentally, the dynamic nuclear polarization has been introduced to study the hyperfine interaction of carrier spins with the nuclear spin bath (Figure 8(c)) [30,115,120]. A pump beam with fixed helicity is used to set the nuclear spin polarization I, which is tilted by an angle φ from the normal to the sample surface, so that a nonzero projection of the carrier spin $S_{e(h)}$ onto the external magnetic field B can be provided. The produced nuclear Overhauser field is $B_{N,e(h)} = A_{e(h)}I / \left(g_{e(h)}\mu_B\right)$, with the direction determined by the sign of the hyperfine coupling constant $A_{e(h)}$, the direction of the nuclear spin polarization I and the carrier g-factors $g_{e(h)}$. Consequently, the Larmor precession frequency of the carrier is modified as $\omega_{L,e(h)} = \left|g_{e(h)}\right|\mu_B\left(B \pm B_{N,e(h)}\right)/\hbar$, which can be used as a measurement of the nuclear effects. Since the pump helicity governs the Overhauser field $B_{N,e(h)}$ by adjusting the carrier spin $S_{e(h)}$, Faraday rotation dynamics with remarkable difference can be observed experimentally by using the

counter-circularly polarized (σ^+ and σ^-) pump light (see Figure 8(d)). The dynamic nuclear polarization effect manifests itself in the hole precession frequency, which changes from 16 rad/ns for σ^- pump to 5 rad/ns for σ^+ pump in $FA_{0.9}Cs_{0.1}PbI_{2.8}Br_{0.2}$ single crystals, and it also exists for the electron causing smaller change in the Larmor frequency though [120]. The stronger Overhauser field experienced by holes than electrons has also been evidenced in bulk $CsPbBr_3$ ($|B_{N,h}|$ = 3.1 mT and $|B_{N,e}|$ = 1.0 mT) [115] and $CsPb(Cl_{0.56}Br_{0.44})_3$ nanocrystals ($|B_{N,h}|$ = 5.8 mT) [30], which is a unique feature of lead halide perovskites due to the inverted band structure compared to the conditional III-V and II-VI semiconductors [130]. Optically detected nuclear magnetic resonance experiments [30,120] together with theoretical analysis [30,115,120] have identified that the ^{207}Pb isotope dominates the hole-nuclei hyperfine interaction, while much more weak coupling exists for the conduction band electrons. As the pump power increases, the nuclear Overhauser field $B_{N,e(h)}$ induced by the optically oriented carriers changes dependently, up to $|B_{N,h}| \approx -50$ mT and $|B_{N,e}| \approx 6$ mT at 1.6 K (see Figure 8(e)) [120]. Additionally, the temperature effect on the Overhauser field is stronger for holes to cause a non-monotonic response, which has been ascribed to the variation of the leakage factor related to the flip-flop process [120].

5. Magnetic field effects in optoelectronic applications

The electron-hole (e-h) pairs inside the perovskite-based optoelectronic devices may recombine radiatively in the form of excitons or dissociate to free carriers to produce photocurrents. They can be divided into parallel and antiparallel spin states with different dissociation and radiative recombination rates by taking the spin configurations into account solely [37]. As a result, the magnetic field-mediated population redistribution of spin sublevels can lead to the modulation of the output physical quantities, such as the photocurrent (PC), electroluminescence (EL), photoluminescence (PL) and resistance [37], laying an essential foundation for understanding the spin-dependent charge-to-photon interconversion dynamics in practical applications [131–135].

It was speculated that the large spin-orbit coupling in lead halide perovskites caused by heavy atom Pb may shorten the spin relaxation time and consequently diminish the magnetic effects [136]. However, Zhang et al. observed remarkable magneto-photocurrent (MPC), magneto-electroluminescence (MEL) and magneto-photoluminescence (MPL) in the $MAPbI_{3-x}Cl_x$ photovoltaic devices and films, as shown in Figure 9(a–c) [37]. The magnetic field effects (MFEs) have been explained by the Δg mechanism (the difference between g_{eff} of electrons and holes) in perovskites, which causes the difference between carrier Larmor precession frequencies to induce spin-mixing significantly before the spin coherence is lost. Moreover, MFEs in perovskite devices with different morphologies were measured to
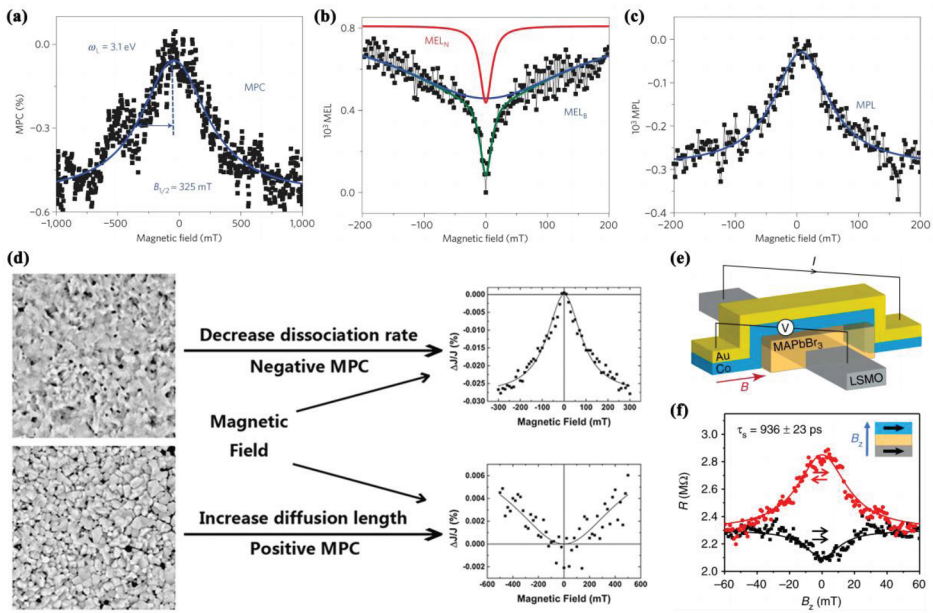
Figure 9. (a) Magneto-photoconductivity (MPC) response measured in the MAPbI$_{3-x}$Cl$_x$ photovoltaic device. (b) Magneto-electroluminescence (MEL) response in the same device as (a) at a constant current of 5 mA showing two components. The broad component (MEL$_B$) fitted by the blue line may originate from the field-induced variation of the non-radiative recombination channel, and the narrow component (MEL$_N$) fitted by the red line may come from the radiative recombination channel. (c) Magneto-photoluminescence (MPL) response of a pristine perovskite film grown in similar conditions to the active layer of device in (a). Reproduced with permission from ref [37]. Copyright 2015, Nature Publishing group. (d) MPC polarity tuned between positive and negative by adjusting the size of the perovskite crystal domain in perovskite films. Reprinted with permission from ref [137]. Copyright 2017, American Chemical Society. (e) Schematic of a LSMO/MAPbBr$_3$/Co spin valve device structure. (f) Hanle effect of the giant magneto-resistance in MAPbBr$_3$-based spin valve. (e) and (f) Reproduced with permission from ref [138]. Copyright 2019, Nature Publishing Group.

unravel that the MFE amplitude and shape should be related to the e-h pair lifetime, which depends on the film morphology [37]. Similarly, Hsiao et al. observed negative MPL and positive MPC in MAPbI$_{3-x}$Cl$_x$ solar cells at low fields under high excitation powers, proving that the charge recombination and dissociation processes are spin dependent [131]. It has been further suggested by Li et al. that the sign of MPC can be regulated by controlling the crystal domains in perovskite films (see Figure 9(d)) [137]. The negative and positive MPC should be dominated by the decreased dissociation rate of spin-antiparallel e-h pairs and the increased diffusion length of spin-parallel e-h pairs in large and small domain structures, respectively. Furthermore, by applying an external magnetic field to Mn-doped CsPbBr$_3$ nanoplates, the photocatalytic efficiency of CO$_2$RR can be greatly improved, which has been attributed to the increased spin-polarized photogenerated carriers, extended carrier lifetime and inhibited charge recombination [139,140].

Lead halide perovskite materials have also shown great potentials in spintronics like spin LEDs and spin valves [141–143]. In the pioneering work, a spin LED that is able to emit circularly polarized light and a vertical spin valve (see Figure 9(e)) that shows giant magneto-resistance have been demonstrated by injecting spin-polarized carriers into MAPbBr$_3$ films from metallic ferromagnetic electrodes [138]. The magneto-resistance response under the transverse field has been observed at both parallel and antiparallel magnetization configurations, as shown in Figure 9(f). This Hanle effect unambiguously confirms the efficient injection and transport of spin-polarized carriers in the device, with the extracted hole spin lifetime of ~ 936 ns and spin diffusion length of ~220 nm.

6. Conclusions and outlook

The magneto-optical effects in lead halide perovskites have been reviewed in this article from fundamental aspects to application development. By means of optical measurements in the magnetic fields, accurate determination of basic physical quantities has been accomplished and the debate concerning the exact ordering of bright triplet and dark singlet exciton states have been settled, rationalizing the efficient charge transport and exciton recombination in perovskite materials as well as the excellent performance of the relevant optoelectronic devices. The carrier spins also show high sensitivity to the external magnetic fields, along with the long spin coherence lifetime, leading to spin quantum-state control in perovskite semiconductors including spin initialization, manipulation and readout in the near future. In-depth analysis of the device working principles has been attempted with the assistance of the magnetic field effects, thus providing unique instructions for designing and optimizing practical applications.

Despite the flourishing and remarkable research in the perovskite community, there still remains several interesting puzzles that might be addressed with magneto-optical spectroscopy. One open question concerns the polaron effects in these structurally soft semiconductors. The quasiparticles may manifest themselves as increased carrier effective mass in the relatively low magnetic field due to the strong Frohlich interaction with specific optical phonons [144,145], and the bare carrier mass can be probed in the high-field regime once the cyclotron motion enables the decoupling from lattice vibrations [39]. An anti-crossing behavior between the Landau levels in the intermediate range can be expected as an elegant proof of the polaron picture in the perovskite materials [36,146,147]. Further, derivatives like 2D layered perovskites might serve as a suitable platform for tailoring the electron-phonon coupling in the form of self-trapped excitons [148,149] or pronounced phonon replicas [48,150–152], which can be flexibly modulated by the quantum and dielectric confinement effects as well as external magnetic fields [48].

Another perovskite counterparts that will benefit from the application of the magnetic fields is the single nanocrystal, which has been regarded as a potential high-performance solid-state quantum light source [28,29,60,62,64]. Based on the efficient biexciton emission, a single perovskite nanocrystal can generate polarization-entangled photon pairs once the bright-exciton fine structure splittings can be eliminated with the magnetic [153–155], electrical [155–157] or strain fields [158,159]. Meanwhile, a charged nanocrystal with an electron or hole trapped inside provides an ideal pathway to realize advanced spin-photon interface, and the external magnetic field plays a vital role in the key steps such as establishing spin states, suppressing spin flip-flop process and manipulating a single spin [160–162]. Furthermore, two non-degenerate circularly polarized trion states formed from the magnetic-field-induced Zeeman effect, together with nanophotonic waveguides, constitute chiral interfaces that lock the local light polarization to its propagation direction [163], enabling the construction of nonreciprocal single-photon devices and deterministic spin-photon interfaces [164,165]. With the advantages of facile synthesis, flexible tunability and convenient integration, the lead halide perovskites are capable of serving as a multifunctional platform for both fundamental research and technology devices, and unique control of the matter qubits with magnetic fields in the soft ionic lattices will offer opportunities for new physics research and applications.

Disclosure statement

References

[1] Protesescu L, Yakunin S, Bodnarchuk MI, et al. Nanocrystals of cesium lead halide perovskites ($CsPbX_3$, X = Cl, Br, and I): novel optoelectronic materials showing bright emission with wide color gamut. Nano Lett. 2015;15:3692–3696. doi: 10.1021/nl5048779

[2] Akkerman QA, D'Innocenzo V, Accornero S, et al. Tuning the optical properties of cesium lead halide perovskite nanocrystals by anion exchange reactions. J Am Chem Soc. 2015;137:10276–10281. doi: 10.1021/jacs.5b05602

[3] De Wolf S, Holovsky J, Moon S-J, et al. Organometallic halide perovskites: Sharp optical absorption edge and its relation to photovoltaic performance. J Phys Chem Lett. 2014;5:1035–1039. doi: 10.1021/jz500279b

[4] Di Stasio F, Christodoulou S, Huo N, et al. Near-unity photoluminescence quantum yield in $CsPbBr_3$ nanocrystal solid-state films via Postsynthesis Treatment with lead bromide. Chem Mater. 2017;29:7663–7667. doi: 10.1021/acs.chemmater.7b02834

[5] Huang H, Susha AS, Kershaw SV, et al. Control of emission color of high quantum yield $CH_3NH_3PbBr_3$ perovskite quantum dots by precipitation temperature. Adv Sci. 2015;2:1500194. doi: 10.1002/advs.201500194

[6] Liu H, Liu Z, Xu W, et al. Engineering the photoluminescence of CsPbX$_3$ (X = Cl, Br, and I) perovskite nanocrystals across the full visible spectra with the interval of 1 nm. ACS Appl Mater Inter. 2019;11:14256–14265. doi: 10.1021/acsami.9b01930

[7] Steirer KX, Schulz P, Teeter G, et al. Defect tolerance in methylammonium lead triiodide perovskite. ACS Energy Lett. 2016;1:360–366. doi: 10.1021/acsenergylett.6b00196

[8] Kang J, Wang L-W. High defect tolerance in lead halide perovskite CsPbBr$_3$. J Phys Chem Lett. 2017;8:489–493. doi: 10.1021/acs.jpclett.6b02800

[9] Huang H, Bodnarchuk MI, Kershaw SV, et al. Lead halide perovskite nanocrystals in the research spotlight: stability and defect tolerance. ACS Energy Lett. 2017;2:2071–2083. doi: 10.1021/acsenergylett.7b00547

[10] de Quilettes DW, Vorpahl SM, Stranks SD, et al. Impact of microstructure on local carrier lifetime in perovskite solar cells. Science. 2015;348:683–686. doi: 10.1126/science.aaa5333

[11] Fu J, Xu Q, Han G, et al. Hot carrier cooling mechanisms in halide perovskites. Nat Commun. 2017;8:1300. doi: 10.1038/s41467-017-01360-3

[12] Yang J, Wen X, Xia H, et al. Acoustic-optical phonon up-conversion and hot-phonon bottleneck in lead-halide perovskites. Nat Commun. 2017;8:14120. doi: 10.1038/ncomms14120

[13] Yang Y, Ostrowski DP, France RM, et al. Observation of a hot-phonon bottleneck in lead-iodide perovskites. Nat Photonics. 2016;10:53–59. doi: 10.1038/nphoton.2015.213

[14] Stranks SD, Eperon GE, Grancini G, et al. Electron-hole diffusion lengths exceeding 1 micrometer in an organometal trihalide perovskite absorber. Science. 2013;342:341–344. doi: 10.1126/science.1243982

[15] Xing G, Mathews N, Sun S, et al. Long-range balanced electron- and hole-transport lengths in organic-inorganic CH$_3$NH$_3$PbI$_3$. Science. 2013;342:344–347. doi: 10.1126/science.1243167

[16] Kojima A, Teshima K, Shirai Y, et al. Organometal halide perovskites as visible-light sensitizers for photovoltaic cells. J Am Chem Soc. 2009;131:6050–6051. doi: 10.1021/ja809598r

[17] Jeong J, Kim M, Seo J, et al. Pseudo-halide anion engineering for α-FAPbI$_3$ perovskite solar cells. Nature. 2021;592:381–385. doi: 10.1038/s41586-021-03406-5

[18] Zhao Y, Ma F, Qu Z, et al. Inactive (PbI$_2$)$_2$RbCl stabilizes perovskite films for efficient solar cells. Science. 2022;377:531–534. doi: 10.1126/science.abp8873

[19] NREL. Best research-cell efficiencies. https://www.nrel.gov/pv/cell-efficiency.html

[20] Hassan Y, Park JH, Crawford ML, et al. Ligand-engineered bandgap stability in mixed-halide perovskite LEDs. Nature. 2021;591:72–77. doi: 10.1038/s41586-021-03217-8

[21] Guo B, Lai R, Jiang S, et al. Ultrastable near-infrared perovskite light-emitting diodes. Nat Photonics. 2022;16:637–643. doi: 10.1038/s41566-022-01046-3

[22] Wu X-G, Ji H, Yan X, et al. Industry outlook of perovskite quantum dots for display applications. Nature Nanotechnol. 2022;17:813–816. doi: 10.1038/s41565-022-01163-8

[23] Zhu H, Fu Y, Meng F, et al. Lead halide perovskite nanowire lasers with low lasing thresholds and high quality factors. Nature Mater. 2015;14:636–642. doi: 10.1038/nmat4271

[24] Dong H, Zhang C, Liu X, et al. Materials chemistry and engineering in metal halide perovskite lasers. Chem Soc Rev. 2020;49:951–982. doi: 10.1039/C9CS00598F

[25] Shang Q, Li M, Zhao L, et al. Role of the exciton–polariton in a continuous-wave optically pumped CsPbBr$_3$ perovskite laser. Nano Lett. 2020;20:6636–6643. doi: 10.1021/acs.nanolett.0c02462

[26] Wang X, Li J, Chen Y, et al. Spray-coating thick films of all-inorganic halide perovskites for filterless narrowband photodetectors. ACS Appl Mater Inter. 2022;14:24583–24591. doi: 10.1021/acsami.2c03585

[27] Li C, Ma Y, Xiao Y, et al. Advances in perovskite photodetectors. InfoMat. 2020;2:1247–1256. doi: 10.1002/inf2.12141

[28] Lv Y, Yin C, Zhang C, et al. Exciton-acoustic phonon coupling revealed by resonant excitation of single perovskite nanocrystals. Nat Commun. 2021;12:2192. doi: 10.1038/s41467-021-22486-5

[29] Utzat H, Sun W, Kaplan AEK, et al. Coherent single-photon emission from colloidal lead halide perovskite quantum dots. Science. 2019;363:1068–1072. doi: 10.1126/science.aau7392

[30] Kirstein E, Kopteva NE, Yakovlev DR, et al. Mode locking of hole spin coherences in CsPb(Cl,Br)$_3$ perovskite nanocrystals. Nat Commun. 2023;14:699. doi: 10.1038/s41467-023-36165-0

[31] Odenthal P, Talmadge W, Gundlach N, et al. Spin-polarized exciton quantum beating in hybrid organic–inorganic perovskites. Nat Phys. 2017;13:894–899. doi: 10.1038/nphys4145

[32] Michler P. Quantum dots for quantum information technologies. Berlin: Springer; 2017.

[33] Žutić I, Fabian J, Das Sarma S. Spintronics: fundamentals and applications. Rev Mod Phys. 2004;76:323–410. doi: 10.1103/RevModPhys.76.323

[34] Yu B, Zhang C, Chen L, et al. Ultrafast dynamics of photoexcited carriers in perovskite semiconductor nanocrystals. Nanophotonics. 2021;10:1943–1965. doi: 10.1515/nanoph-2020-0681

[35] Baranowski M, Plochocka P. Excitons in metal-halide perovskites. Adv Energy Mater. 2020;10:1903659. doi: 10.1002/aenm.201903659

[36] Surrente A, Baranowski M, Plochocka P. Perspective on the physics of two-dimensional perovskites in high magnetic field. Appl Phys Lett. 2021;118:170501. doi: 10.1063/5.0048490

[37] Zhang C, Sun D, Sheng CX, et al. Magnetic field effects in hybrid perovskite devices. Nat Phys. 2015;11:427–434. doi: 10.1038/nphys3277

[38] Yu ZG. Effective-mass model and magneto-optical properties in hybrid perovskites. Sci Rep. 2016;6:28576. doi: 10.1038/srep28576

[39] Miura N. Physics of semiconductors in high magnetic fields. New York: OUP Oxford; 2007.

[40] Tanaka K, Takahashi T, Ban T, et al. Comparative study on the excitons in lead-halide-based perovskite-type crystals $CH_3NH_3PbBr_3$ $CH_3NH_3PbI_3$. Solid State Commun. 2003;127:619–623. doi: 10.1016/S0038-1098(03)00566-0

[41] Galkowski K, Mitioglu A, Miyata A, et al. Determination of the exciton binding energy and effective masses for methylammonium and formamidinium lead tri-halide perovskite semiconductors. Energy Environ Sci. 2016;9:962–970. doi: 10.1039/C5EE03435C

[42] Mahboubi Soufiani A, Yang Z, Young T, et al. Impact of microstructure on the electron–hole interaction in lead halide perovskites. Energy Environ Sci. 2017;10:1358–1366. doi: 10.1039/C7EE00685C

[43] Kataoka T, Kondo T, Ito R, et al. Magneto-optical study on excitonic spectra in $(C_6H_{13}NH_3)_2PbI_4$. Phys Rev B. 1993;47:2010–2018. doi: 10.1103/PhysRevB.47.2010

[44] Stier AV, Wilson NP, Velizhanin KA, et al. Magnetooptics of exciton Rydberg states in a monolayer semiconductor. *Phys Rev Lett*. 2018;120:057405. doi: 10.1103/PhysRevLett.120.057405

[45] Hirasawa M, Ishihara T, Goto T, et al. Magnetoabsorption of the lowest exciton in perovskite-type compound $(CH_3NH_3)PbI_3$. Phys B Condens Matter. 1994;201:427–430. doi: 10.1016/0921-4526(94)91130-4

[46] Baranowski M, Plochocka P, Su R, et al. Exciton binding energy and effective mass of CsPbCl$_3$: a magneto-optical study. Photonics Res. 2020;8:A50. doi: 10.1364/PRJ.401872

[47] Blancon JC, Stier AV, Tsai H, et al. Scaling law for excitons in 2D perovskite quantum wells. Nat Commun. 2018;9:2254. doi: 10.1038/s41467-018-04659-x

[48] Baranowski M, Zelewski SJ, Kepenekian M, et al. Phase-transition-induced carrier mass enhancement in 2D ruddlesden–popper perovskites. ACS Energy Lett. 2019;4:2386–2392. doi: 10.1021/acsenergylett.9b01435

[49] Makado PC, McGill NC. Energy levels of a neutral hydrogen-like system in a constant magnetic field of arbitrary strength. J Phys C. 1986;19:873–885. doi: 10.1088/0022-3719/19/6/008

[50] Miyata A, Mitioglu A, Plochocka P, et al. Direct measurement of the exciton binding energy and effective masses for charge carriers in organic–inorganic tri-halide perovskites. Nat Phys. 2015;11:582–587. doi: 10.1038/nphys3357

[51] Yang Z, Surrente A, Galkowski K, et al. Unraveling the exciton binding energy and the dielectric constant in single-crystal methylammonium lead triiodide perovskite. J Phys Chem Lett. 2017;8:1851–1855. doi: 10.1021/acs.jpclett.7b00524

[52] Gałkowski K, Surrente A, Baranowski M, et al. Excitonic properties of low-band-gap lead–tin halide perovskites. *ACS Energy Lett.* 2019;4:615–621. doi: 10.1021/acsenergylett.8b02243

[53] Yang Z, Surrente A, Galkowski K, et al. Impact of the halide cage on the electronic properties of fully inorganic cesium lead halide perovskites. ACS Energy Lett. 2017;2:1621–1627. doi: 10.1021/acsenergylett.7b00416

[54] Dyksik M, Duim H, Zhu X, et al. Broad tunability of carrier effective masses in two-dimensional halide perovskites. ACS Energy Lett. 2020;5:3609–3616. doi: 10.1021/acsenergylett.0c01758

[55] Even J, Pédesseau L, Katan C. Analysis of multivalley and multibandgap absorption and enhancement of free carriers related to exciton screening in hybrid perovskites. J Phys Chem C. 2014;118:11566–11572. doi: 10.1021/jp503337a

[56] Tan ZK, Moghaddam RS, Lai ML, et al. Bright light-emitting diodes based on organometal halide perovskite. Nat Nanotech. 2014;9:687–692. doi: 10.1038/nnano.2014.149

[57] Miyauchi Y, Iwamura M, Mouri S, et al. Brightening of excitons in carbon nanotubes on dimensionality modification. Nat Photonics. 2013;7:715–719. doi: 10.1038/nphoton.2013.179

[58] Bester G, Nair S, Zunger A. Pseudopotential calculation of the excitonic fine structure of million-atom self-assembled In$_{1-x}$Ga$_x$As/GaAs quantum dots. Phys Rev B. 2003;67:161306. doi: 10.1103/PhysRevB.67.161306

[59] Nirmal M, Norris DJ, Kuno M, et al. Observation of the "dark exciton" in CdSe quantum dots. *Phys Rev Lett.* 1995;75:3728–3731. doi: 10.1103/PhysRevLett.75.3728

[60] Yin C, Chen L, Song N, et al. Bright-exciton fine-structure splittings in single perovskite nanocrystals. *Phys Rev Lett.* 2017;119:026401. doi: 10.1103/PhysRevLett.119.026401

[61] Hou L, Tamarat P, Lounis B. Revealing the exciton fine structure in lead halide perovskite nanocrystals. Nanomaterials. 2021;11:1058. doi: 10.3390/nano11041058

[62] Lv B, Zhu T, Tang Y, et al. Probing permanent dipole moments and removing exciton fine structures in single perovskite nanocrystals by an electric field. *Phys Rev Lett.* 2021;126:197403. doi: 10.1103/PhysRevLett.126.197403

[63] Tamarat P, Bodnarchuk MI, Trebbia J-B, et al. The ground exciton state of formamidinium lead bromide perovskite nanocrystals is a singlet dark state. Nature Mater. 2019;18:717–724. doi: 10.1038/s41563-019-0364-x

[64] Tamarat P, Hou L, Trebbia J-B, et al. The dark exciton ground state promotes photon-pair emission in individual perovskite nanocrystals. Nat Commun. 2020;11:6001. doi: 10.1038/s41467-020-19740-7

[65] Tamarat P, Prin E, Berezovska Y, et al. Universal scaling laws for charge-carrier interactions with quantum confinement in lead-halide perovskites. Nat Commun. 2023;14:229. doi: 10.1038/s41467-023-35842-4

[66] Correa-Baena J-P, Saliba M, Buonassisi T, et al. Promises and challenges of perovskite solar cells. Science. 2017;358:739–744. doi: 10.1126/science.aam6323

[67] Zhu HL, Cheng J, Zhang D, et al. Room-temperature solution-processed NiO_x: PbI_2 nanocomposite structures for realizing high-performance perovskite photodetectors. ACS Nano. 2016;10:6808–6815. doi: 10.1021/acsnano.6b02425

[68] Xu Y, Chen Q, Zhang C, et al. Two-photon-pumped perovskite semiconductor nanocrystal lasers. J Am Chem Soc. 2016;138:3761–3768. doi: 10.1021/jacs.5b12662

[69] Lv Y, Yin C, Zhang C, et al. Quantum interference in a single perovskite nanocrystal. Nano Lett. 2019;19:4442–4447. doi: 10.1021/acs.nanolett.9b01237

[70] Cao Z, Hu F, Zhang C, et al. Optical studies of semiconductor perovskite nanocrystals for classical optoelectronic applications and quantum information technologies: a review. Adv Photon. 2020;2:054001. doi: 10.1117/1.AP.2.5.054001

[71] Endres J, Egger DA, Kulbak M, et al. Valence and conduction band densities of states of metal halide perovskites: a combined experimental–theoretical study. J Phys Chem Lett. 2016;7:2722–2729. doi: 10.1021/acs.jpclett.6b00946

[72] Even J, Pedesseau L, Jancu J-M, et al. Importance of spin–orbit coupling in hybrid organic/inorganic perovskites for photovoltaic applications. J Phys Chem Lett. 2013;4:2999–3005. doi: 10.1021/jz401532q

[73] Brivio F, Butler KT, Walsh A, et al. Relativistic quasiparticle self-consistent electronic structure of hybrid halide perovskite photovoltaic absorbers. Phys Rev B. 2014;89:155204. doi: 10.1103/PhysRevB.89.155204

[74] Karlsson KF, Dupertuis MA, Oberli DY, et al. Fine structure of exciton complexes in high-symmetry quantum dots: effects of symmetry breaking and symmetry elevation. Phys Rev B. 2010;81:161307. doi: 10.1103/PhysRevB.81.161307

[75] Nestoklon MO, Goupalov SV, Dzhioev RI, et al. Optical orientation and alignment of excitons in ensembles of inorganic perovskite nanocrystals. Phys Rev B. 2018;97:235304. doi: 10.1103/PhysRevB.97.235304

[76] Yin C, Lv Y, Zhang X, et al. Transition from doublet to triplet excitons in single perovskite nanocrystals. J Phys Chem Lett. 2020;11:5750–5755. doi: 10.1021/acs.jpclett.0c01939

[77] Rashba EI, Sherman EY. Spin-orbital band splitting in symmetric quantum wells. Phys Lett A. 1988;129:175–179. doi: 10.1016/0375-9601(88)90140-5

[78] Mosconi E, Etienne T, De Angelis F. Rashba band splitting in organohalide lead perovskites: bulk and surface effects. J Phys Chem Lett. 2017;8:2247–2252. doi: 10.1021/acs.jpclett.7b00328

[79] Sercel PC, Lyons JL, Wickramaratne D, et al. Exciton fine structure in perovskite nanocrystals. Nano Lett. 2019;19:4068–4077. doi: 10.1021/acs.nanolett.9b01467

[80] Niesner D, Wilhelm M, Levchuk I, et al. Giant Rashba splitting in $CH_3NH_3PbBr_3$ organic-inorganic perovskite. *Phys Rev Lett*. 2016;117:126401. doi: 10.1103/PhysRevLett.117.126401

[81] Etienne T, Mosconi E, De Angelis F. Dynamical origin of the Rashba effect in organohalide lead perovskites: a key to suppressed carrier recombination in perovskite solar cells? J Phys Chem Lett. 2016;7:1638–1645. doi: 10.1021/acs.jpclett.6b00564

[82] Fernée MJ, Tamarat P, Lounis B. Spectroscopy of single nanocrystals. Chem Soc Rev. 2014;43:1311–1337. doi: 10.1039/c3cs60209e

[83] Chen L, Li B, Zhang C, et al. Composition-dependent energy splitting between bright and dark excitons in lead halide perovskite nanocrystals. Nano Lett. 2018;18:2074–2080. doi: 10.1021/acs.nanolett.8b00184

[84] Bayer M, Ortner G, Stern O, et al. Fine structure of neutral and charged excitons in self-assembled in(Ga)As/(al)gaas quantum dots. Phys Rev B. 2002;65:195315. doi: 10.1103/PhysRevB.65.195315

[85] Canneson D, Shornikova EV, Yakovlev DR, et al. Negatively charged and dark excitons in $CsPbBr_3$ perovskite nanocrystals revealed by high magnetic fields. Nano Lett. 2017;17:6177–6183. doi: 10.1021/acs.nanolett.7b02827

[86] Sercel PC, Lyons JL, Bernstein N, et al. Quasicubic model for metal halide perovskite nanocrystals. J Chem Phys. 2019;151:234106. doi: 10.1063/1.5127528

[87] Fu M, Tamarat P, Trebbia J-B, et al. Unraveling exciton–phonon coupling in individual $FAPbI_3$ nanocrystals emitting near-infrared single photons. Nat Commun. 2018;9:3318. doi: 10.1038/s41467-018-05876-0

[88] Posmyk K, Zawadzka N, Dyksik M, et al. Quantification of exciton fine structure splitting in a two-dimensional perovskite compound. J Phys Chem Lett. 2022;13:4463–4469. doi: 10.1021/acs.jpclett.2c00942

[89] Neumann T, Feldmann S, Moser P, et al. Manganese doping for enhanced magnetic brightening and circular polarization control of dark excitons in paramagnetic layered hybrid metal-halide perovskites. Nat Commun. 2021;12:3489. doi: 10.1038/s41467-021-23602-1

[90] Dyksik M, Duim H, Maude DK, et al. Brightening of dark excitons in 2D perovskites. Sci Adv. 2021;7:eabk0904. doi: 10.1126/sciadv.abk0904

[91] Ema K, Umeda K, Toda M, et al. Huge exchange energy and fine structure of excitons in an organic-inorganic quantum well material. Phys Rev B. 2006;73:241310. doi: 10.1103/PhysRevB.73.241310

[92] Baranowski M, Galkowski K, Surrente A, et al. Giant fine structure splitting of the bright exciton in a bulk $MAPbBr_3$ single crystal. Nano Lett. 2019;19:7054–7061. doi: 10.1021/acs.nanolett.9b02520

[93] Do TTH, Granados Del Águila A, Zhang D, et al. Bright exciton fine-structure in two-dimensional lead halide perovskites. Nano Lett. 2020;20:5141–5148. doi: 10.1021/acs.nanolett.0c01364

[94] Bonadeo NH, Erland J, Gammon D, et al. Coherent optical control of the quantum state of a single quantum dot. Science. 1998;282:1473–1476. doi: 10.1126/science.282.5393.1473

[95] Li X, Wu Y, Steel D, et al. An all-optical quantum gate in a semiconductor quantum dot. Science. 2003;301:809–811. doi: 10.1126/science.1083800

[96] Fu M, Tamarat P, Huang H, et al. Neutral and charged exciton fine structure in single lead halide perovskite nanocrystals revealed by magneto-optical spectroscopy. Nano Lett. 2017;17:2895–2901. doi: 10.1021/acs.nanolett.7b00064

[97] Long G, Jiang C, Sabatini R, et al. Spin control in reduced-dimensional chiral perovskites. Nat Photonics. 2018;12:528–533. doi: 10.1038/s41566-018-0220-6

[98] Isarov M, Tan LZ, Bodnarchuk MI, et al. Rashba effect in a single colloidal $CsPbBr_3$ perovskite nanocrystal detected by magneto-optical measurements. Nano Lett. 2017;17:5020–5026. doi: 10.1021/acs.nanolett.7b02248

[99] Mante P-A, Stoumpos CC, Kanatzidis MG, et al. Electron–acoustic phonon coupling in single crystal $CH_3NH_3PbI_3$ perovskites revealed by coherent acoustic phonons. Nat Commun. 2017;8:14398. doi: 10.1038/ncomms14398

[100] Wright AD, Verdi C, Milot RL, et al. Electron–phonon coupling in hybrid lead halide perovskites. Nat Commun. 2016;7:11755. doi: 10.1038/ncomms11755

[101] Poncé S, Schlipf M, Giustino F. Origin of low carrier mobilities in halide perovskites. ACS Energy Lett. 2019;4:456–463. doi: 10.1021/acsenergylett.8b02346

[102] Urban JM, Chehade G, Dyksik M, et al. Revealing excitonic phonon coupling in $(PEA)_2(MA)_{n-1}Pb_nI_{3n+1}$ 2D layered perovskites. J Phys Chem Lett. 2020;11:5830–5835. doi: 10.1021/acs.jpclett.0c01714

[103] Song F, Qian C, Wang Y, et al. Hot Polarons with trapped excitons and octahedra-twist phonons in $CH_3NH_3PbBr_3$ hybrid perovskite nanowires. Laser Photonics Rev. 2020;14:1900267. doi: 10.1002/lpor.201900267

[104] Neukirch AJ, Nie W, Blancon J-C, et al. Polaron stabilization by cooperative lattice distortion and cation rotations in hybrid perovskite materials. Nano Lett. 2016;16:3809–3816. doi: 10.1021/acs.nanolett.6b01218

[105] Miyata K, Atallah TL, Zhu XY. Lead halide perovskites: crystal-liquid duality, phonon glass electron crystals, and large polaron formation. Sci Adv. 2017;3:e1701469. doi: 10.1126/sciadv.1701469

[106] Frost JM, Whalley LD, Walsh A. Slow cooling of hot polarons in halide perovskite solar cells. ACS Energy Lett. 2017;2:2647–2652. doi: 10.1021/acsenergylett.7b00862

[107] Bretschneider SA, Ivanov I, Wang HI, et al. Quantifying polaron formation and charge carrier cooling in lead-iodide perovskites. Adv Mater. 2018;30:1707312. doi: 10.1002/adma.201707312

[108] Park M, Neukirch AJ, Reyes-Lillo SE, et al. Excited-state vibrational dynamics toward the polaron in methylammonium lead iodide perovskite. Nat Commun. 2018;9:2525. doi: 10.1038/s41467-018-04946-7

[109] Puppin M, Polishchuk S, Colonna N, et al. Evidence of large polarons in photoemission band mapping of the perovskite semiconductor $CsPbBr_3$. *Phys Rev Lett*. 2020;124:206402. doi: 10.1103/PhysRevLett.124.206402

[110] Field RW. Spectra and dynamics of small molecules: alexander von Humboldt Lectures. Springer International Publishing; 2015. doi:10.1007/978-3-319-15958-4

[111] Khaetskii AV. Spin physics in semiconductors. Berlin: Springer; 2017.

[112] Strohmair S, Dey A, Tong Y, et al. Spin polarization dynamics of free charge carriers in $CsPbI_3$ nanocrystals. Nano Lett. 2020;20:4724–4730. doi: 10.1021/acs.nanolett.9b05325

[113] Giovanni D, Ma H, Chua J, et al. Highly spin-polarized carrier dynamics and ultralarge photoinduced magnetization in $CH_3NH_3PbI_3$ perovskite thin films. Nano Lett. 2015;15:1553–1558. doi: 10.1021/nl5039314

[114] Li Y, Luo X, Liu Y, et al. Size- and composition-dependent exciton spin relaxation in lead halide perovskite quantum dots. ACS Energy Lett. 2020;5:1701–1708. doi: 10.1021/acsenergylett.0c00525

[115] Belykh VV, Yakovlev DR, Glazov MM, et al. Coherent spin dynamics of electrons and holes in $CsPbBr_3$ perovskite crystals. Nat Commun. 2019;10:673. doi: 10.1038/s41467-019-08625-z

[116] Crane MJ, Jacoby LM, Cohen TA, et al. Coherent spin precession and lifetime-limited spin dephasing in $CsPbBr_3$ perovskite nanocrystals. Nano Lett. 2020;20:8626–8633. doi: 10.1021/acs.nanolett.0c03329

[117] Grigoryev PS, Belykh VV, Yakovlev DR, et al. Coherent spin dynamics of electrons and holes in $CsPbBr_3$ colloidal nanocrystals. Nano Lett. 2021;21:8481–8487. doi: 10.1021/acs.nanolett.1c03292

[118] Privitera A, Righetto M, Cacialli F, et al. Perspectives of organic and perovskite-based Spintronics. Adv Opt Mater. 2021;9:2100215. doi: 10.1002/adom.202100215

[119] Kepenekian M, Even J. Rashba and Dresselhaus Couplings in halide perovskites: accomplishments and opportunities for Spintronics and spin–orbitronics. J Phys Chem Lett. 2017;8:3362–3370. doi: 10.1021/acs.jpclett.7b01015

[120] Kirstein E, Yakovlev DR, Glazov MM, et al. Lead-dominated hyperfine interaction impacting the carrier spin dynamics in halide perovskites. Adv Mater. 2022;34:2105263. doi: 10.1002/adma.202105263

[121] Kirstein E, Yakovlev DR, Glazov MM, et al. The Landé factors of electrons and holes in lead halide perovskites: universal dependence on the band gap. Nat Commun. 2022;13:3062. doi: 10.1038/s41467-022-30701-0

[122] Kopteva N, Yakovlev D, Kirstein E, et al. Weak dispersion of exciton landé factor with band gap energy in lead halide perovskites: approximate compensation of the electron and hole dependences. 2023; arXiv preprint arXiv:2301.12775 2023.

[123] Glazov MM. Coherent spin dynamics of electrons and excitons in nanostructures (a review). Phys Solid State. 2012;54:1–27. doi: 10.1134/S1063783412010143

[124] Nowack KC, Koppens FHL, Nazarov YV, et al. Coherent control of a single electron spin with electric fields. Science. 2007;318:1430–1433. doi: 10.1126/science.1148092

[125] Koppens FHL, Buizert C, Tielrooij KJ, et al. Driven coherent oscillations of a single electron spin in a quantum dot. Nature. 2006;442:766–771. doi: 10.1038/nature05065

[126] Lin X, Han Y, Zhu J, et al. Room-temperature coherent optical manipulation of hole spins in solution-grown perovskite quantum dots. Nature Nanotechnol. 2023;18:124–130. doi: 10.1038/s41565-022-01279-x

[127] Dyakonov MI. Basics of Semiconductor and Spin Physics. Spin Physics in Semiconductors. Berlin: Springer; 2017.

[128] Bloembergen N. Nuclear magnetic relaxation in semiconductors. Physica. 1954;20:1130–1133. doi: 10.1016/S0031-8914(54)80253-9

[129] Schimpf AM, Ochsenbein ST, Gamelin DR. Surface contributions to Mn^{2+} spin dynamics in colloidal doped quantum dots. J Phys Chem Lett. 2015;6:457–463. doi: 10.1021/jz5026678

[130] Chekhovich EA, Glazov MM, Krysa AB, et al. Element-sensitive measurement of the hole–nuclear spin interaction in quantum dots. Nat Phys. 2013;9:74–78. doi: 10.1038/nphys2514

[131] Hsiao Y-C, Wu T, Li M, et al. Magneto-optical studies on spin-dependent charge recombination and dissociation in perovskite solar cells. Adv Mater. 2015;27:2899–2906. doi: 10.1002/adma.201405946

[132] Xu H, Wang M, Yu Z-G, et al. Magnetic field effects on excited states, charge transport, and electrical polarization in organic semiconductors in spin and orbital regimes. Adv Phys. 2019;68:49–121. doi: 10.1080/00018732.2019.1590295

[133] Pavliuk MV, Fernandes DLA, El-Zohry AM, et al. Magnetic manipulation of spontaneous emission from inorganic $CsPbBr_3$ perovskites nanocrystals. Advanced Optical Materials. 2016;4:2004–2008. doi: 10.1002/adom.201600611

[134] Zhang K, Zhao J, Hu Q, et al. Room-temperature magnetic field effect on excitonic photoluminescence in perovskite nanocrystals. Adv Mater. 2021;33:2008225. doi: 10.1002/adma.202008225

[135] Pham MT, Amerling E, Luong HM, et al. Origin of Rashba spin-orbit coupling in 2D and 3D lead iodide perovskites. Sci Rep. 2020;10:4964. doi: 10.1038/s41598-020-61768-8

[136] Devir-Wolfman AH, Khachatryan B, Gautam BR, et al. Short-lived charge-transfer excitons in organic photovoltaic cells studied by high-field magneto-photocurrent. Nat Commun. 2014;5:4529. doi: 10.1038/ncomms5529

[137] Li W, Yuan S, Zhan Y, et al. Tuning magneto-photocurrent between positive and negative polarities in perovskite solar cells. J Phys Chem C. 2017;121:9537–9542. doi: 10.1021/acs.jpcc.7b00571

[138] Wang J, Zhang C, Liu H, et al. Spin-optoelectronic devices based on hybrid organic-inorganic trihalide perovskites. Nat Commun. 2019;10:129. doi: 10.1038/s41467-018-07952-x

[139] Wang Z, Li Y, Wu C, et al. Electric-/magnetic-field-assisted photocatalysis: mechanisms and design strategies. Joule. 2022;6:1798–1825. doi: 10.1016/j.joule.2022.06.018

[140] Lin C-C, Liu T-R, Lin S-R, et al. Spin-polarized photocatalytic CO_2 reduction of Mn-doped perovskite nanoplates. J Am Chem Soc. 2022;144:15718–15726. doi: 10.1021/jacs.2c06060

[141] Liao K, Hu X, Cheng Y, et al. Spintronics of hybrid organic–inorganic perovskites: miraculous basis of integrated optoelectronic devices. Adv Opt Mater. 2019;7:1900350. doi: 10.1002/adom.201900350

[142] Kim Y-H, Zhai Y, Lu H, et al. Chiral-induced spin selectivity enables a room-temperature spin light-emitting diode. Science. 2021;371:1129–1133. doi: 10.1126/science.abf5291

[143] Lu H, Wang J, Xiao C, et al. Spin-dependent charge transport through 2D chiral hybrid lead-iodide perovskites. Sci Adv. 2019;5:eaay0571. doi: 10.1126/sciadv.aay0571

[144] Feynman RP. Slow electrons in a polar crystal. Phys Rev. 1955;97:660–665. doi: 10.1103/PhysRev.97.660

[145] Polarons ED. Cambridge University Press; 2013. 10.1017/CBO9781139023436

[146] Najda SP, Yokoi H, Takeyama S, et al. Infrared magnetospectroscopy of n-type InP at magnetic fields up to 150 T. Phys Rev B. 1991;44:1087–1091. doi: 10.1103/PhysRevB.44.1087

[147] Najda SP, Takeyama S, Miura N, et al. Infrared magnetospectroscopy of GaAs at magnetic fields up to 150 T. Phys Rev B. 1989;40:6189–6195. doi: 10.1103/PhysRevB.40.6189

[148] Li S, Luo J, Liu J, et al. Self-trapped excitons in all-inorganic halide perovskites: fundamentals, status, and potential applications. J Phys Chem Lett. 2019;10:1999–2007. doi: 10.1021/acs.jpclett.8b03604

[149] Smith MD, Karunadasa HI. White-light emission from layered halide perovskites. *Acc Chem Res*. 2018;51:619–627. doi: 10.1021/acs.accounts.7b00433

[150] Ni L, Huynh U, Cheminal A, et al. Real-time observation of exciton–phonon coupling dynamics in self-assembled hybrid perovskite quantum wells. ACS Nano. 2017;11:10834–10843. doi: 10.1021/acsnano.7b03984

[151] Neutzner S, Thouin F, Cortecchia D, et al. Exciton-polaron spectral structures in two-dimensional hybrid lead-halide perovskites. Phys Rev Mater. 2018;2:064605. doi: 10.1103/PhysRevMaterials.2.064605

[152] Gong X, Voznyy O, Jain A, et al. Electron–phonon interaction in efficient perovskite blue emitters. Nature Mater. 2018;17:550–556. doi: 10.1038/s41563-018-0081-x

[153] Tokman M, Yao X, Belyanin A. Generation of entangled photons in graphene in a strong magnetic field. *Phys Rev Lett*. 2013;110:077404. doi: 10.1103/PhysRevLett.110.077404

[154] Stevenson RM, Young RJ, See P, et al. Magnetic-field-induced reduction of the exciton polarization splitting in InAs quantum dots. Phys Rev B. 2006;73:033306. doi: 10.1103/PhysRevB.73.033306

[155] Pooley MA, Bennett AJ, Stevenson RM, et al. Energy-tunable quantum dot with minimal fine structure created by using Simultaneous electric and magnetic fields. *Phys Rev Appl*. 2014;1:024002. doi: 10.1103/PhysRevApplied.1.024002

[156] Ghali M, Ohtani K, Ohno Y, et al. Generation and control of polarization-entangled photons from GaAs island quantum dots by an electric field. Nat Commun. 2012;3:661. doi: 10.1038/ncomms1657

[157] Huber D, Reindl M, Aberl J, et al. Semiconductor quantum dots as an ideal source of polarization-entangled photon pairs on-demand: a review. J Opt. 2018;20:073002. doi: 10.1088/2040-8986/aac4c4

[158] Zhang J, Wildmann JS, Ding F, et al. High yield and ultrafast sources of electrically triggered entangled-photon pairs based on strain-tunable quantum dots. Nat Commun. 2015;6:10067. doi: 10.1038/ncomms10067

[159] Jin T, Li X, Liu R, et al. Generation of polarization-entangled photons from self-assembled quantum dots in a hybrid quantum photonic chip. Nano Lett. 2022;22:586–593. doi: 10.1021/acs.nanolett.1c03226

[160] Warburton RJ. Single spins in self-assembled quantum dots. Nature Mater. 2013;12:483–493. doi: 10.1038/nmat3585

[161] Berezovsky J, Mikkelsen MH, Stoltz NG, et al. Picosecond coherent optical manipulation of a single electron spin in a quantum dot. Science. 2008;320:349–352. doi: 10.1126/science.1154798

[162] Emary C, Xu X, Steel DG, et al. Fast initialization of the spin state of an electron in a quantum dot in the Voigt configuration. *Phys Rev Lett*. 2007;98:047401. doi: 10.1103/PhysRevLett.98.047401

[163] Lodahl P, Mahmoodian S, Stobbe S, et al. Chiral quantum optics. Nature. 2017;541:473–480. doi: 10.1038/nature21037

[164] Söllner I, Mahmoodian S, Hansen SL, et al. Deterministic photon–emitter coupling in chiral photonic circuits. Nature Nanotechnol. 2015;10:775–778. doi: 10.1038/nnano.2015.159

[165] Coles RJ, Price DM, Dixon JE, et al. Chirality of nanophotonic waveguide with embedded quantum emitter for unidirectional spin transfer. Nat Commun. 2016;7:11183. doi: 10.1038/ncomms11183